Investigation of two-electron ORR pathway of non-metallic carbon-based catalysts with P-C bond structure in Cl⁻-bearing electrolytes

Qiuchen He , Jiangpeng Li, Yuchen Qiao, Su Zhan [*], Feng Zhou [*]

Dalian Maritime University, Key Lab Ship. Machinery Maintenance & Manufacture, Minist. Transport, Dalian 116026, Peoples Republic of China

A B S T R A C T

On-site small-scale synthesis of H_2O_2 using an electrocatalytic reaction with seawater and air as feedstock is crucial for the Fenton reaction to handle marine pollution. However, the reaction is severely constrained by the poisonous effects of excess Cl⁻ in seawater on the 2e⁻ oxygen reduction reaction (ORR) center, necessitating the development of catalysts with high activity and chlorine tolerance. In this study, a catalyst with a high H_2O_2 yield of 3.33 $molg^{-1}h^{-1}$ was developed with P-C bond structures whose active center was not only unaffected by Cl⁻ but also promoted the reduction of O_2 to H_2O_2 in the 2e⁻ path when adsorbed Cl⁻ was present. The H_2O_2 produced in real seawater completely inactivated the algal microorganisms in the flow cell within 10 min. Our results could advance technologies for reducing marine pollution and serve as a guide for the design of catalysts used in Cl⁻-bearing electrolytes.

1. Introduction

The control of marine pollution has become important due to the growth of global industry and the escalating severity of the marine pollution problem. The Fenton reaction is an effective method of controlling marine pollution. The hydroxyl radicals (•OH) produced by the Fenton reaction can eliminate vermin, other organic contaminants, and marine oil pollution [1–4]. They can also render hazardous marine microbes inactive, preventing biological invasion. However, the main issue with this technology is how to address the issue of the H_2O_2 source. The traditional anthraquinone method of producing H_2O_2 needs expensive equipment, and the high concentration of the H_2O_2 solution produced causes difficulty with storage and transportation at sea [5,6]. As a result, relying on the large-scale production of H_2O_2 in factories is not a feasible solution to control marine pollution. The use of the electrocatalytic 2e⁻ oxygen reduction reaction (ORR) for the direct synthesis of H_2O_2 on a small-scale on-site in the marine environment can avoid the use of expensive equipment while removing the potential risk of storing and transporting high concentrations of H_2O_2. This technology is an efficient method for addressing the H_2O_2 source.

The electrocatalytic synthesis of H_2O_2 has progressed significantly over the past few decades, researchers have focused their efforts on nonprecious metal catalysts. For instance, Co-based monatomic catalysts have proven to be promising 2e⁻ ORR catalysts for applications because of their distinctive geometry and electronic structure [7], which are favorable for O_2 adsorption activation and can efficiently reduce the thermodynamic potential barrier from $*O_2$ to $*OOH$. They also have a moderate adsorption capacity for the intermediate product $*OOH$ without further decomposition of $*OOH$ into $*O$ and $*OH$, resulting in high H_2O_2 selectivity [8,9]. By modifying the coordination environment of the Co-based single atom to further lower the kinetic barrier of its 2e⁻ ORR [10], it is anticipated that the catalytic performance will be further enhanced. Co-based single-atom catalysts can produce H_2O_2 with good selectivity in a variety of electrolytes, including KOH, Na_2SO_4, and H_2SO_4. Nevertheless, unlike ordinary electrolytes, the marine environment contains a significant amount of NaCl, and Cl⁻ is believed to have a potent deleterious effect on metal catalysts. Since Cl⁻ is a strong adsorbing anion, it adsorbs to metal sites, competing with O_2 adsorption and even blocking O_2 adsorption [11]. Although the coordination structure of Co can be slightly altered to improve the selective adsorption of O_2 in NaCl solution, the harmful effects of Cl⁻ are not fully avoidable. Therefore, for electrocatalytic processes in marine environments, the design of 2e⁻ ORR catalysts that can withstand Cl⁻ is crucial.

In marine environments, nonmetallic carbon-based catalysts are preferable to metallic monoatomic catalysts. It has been demonstrated that carbon-based catalysts exhibit some chlorine resistance and even show improved ORR performance in electrolytes containing Cl⁻ [12]. This potentially occurs because Cl⁻ adsorption causes the electrons on

---

* Corresponding authors.
  E-mail addresses: zhans@dlmu.edu.cn (S. Zhan), zhoufeng@dlmu.edu.cn (F. Zhou).

the carbon surface to rearrange, forming positively charged regions on nearby carbon atoms and promote the adsorption and activation of O_2 on its sites. However, compared to catalysts containing metals, the intrinsic activity of carbon-based catalysts is lower [13]. The application of nonmetallic heteroatom doping breaks the conjugated bonds and redistributes the electrons on the surface of carbon materials; this process results in increased O_2 adsorption performance and the binding energy with intermediates (*OOH), considerably increasing the ORR selectivity and activity [14,15]. One of the most researched techniques is N doping, where N is found in the carbon structure as graphitic nitrogen (graphitic N), pyridinic nitrogen (pyridinic N), and pyrrolic nitrogen (pyrrolic N). Graphitic N and pyrrolic N are generally considered to be structures that promote the 2e⁻ ORR pathway [16–20], and pyridinic N promotes the 4e⁻ ORR process [21,22]. Fernandez-Escamilla et al. [23] suggested via DFT calculations that the reduction pathway of the oxygen in pyridinic N was related to the form of pyridinic N arrangement, and O_2 was also reduced in the 2e⁻ pathway when three pyridinic N atoms were adjacent to each other. However, the content, present form, and distribution of nitrogen within the carbon material are difficult to accurately tune during the actual catalytic reaction, which may result in a low 2e⁻ ORR selectivity of partially nitrogen-doped carbon. Nonetheless, this work suggests that the coordination environment of the nonmetal carbon-based catalyst plays a crucial role in controlling the ORR pathway.

P is frequently added to carbon materials to enhance their ORR characteristics in addition to N doping. In contrast to N, the electronegativity of P (2.19) is smaller than that of C (2.55), the surface of P atom is positively charged, and O_2 is adsorbed on it (which is called the Griffith-type, in which two oxygen atoms are side-adsorbed on the P site), causing the site to strongly activate O_2. Because the intermediate product of the ORR process, *OOH, could be disassociated by the active site effect and form *O and *OH, this structure is frequently used in 4e⁻ ORR studies [24–26]. However, considering the unique usage environment of seawater, after P is poisoned by Cl⁻, its adsorption ability to O_2 and *OOH changes. The reaction path of ORR at the P site then switches from the 4e⁻ path to the 2e⁻ path if this property is reasonably used.

In our study, P-doped carbon materials were successfully synthesized and loaded onto an electrode with a gas diffusion layer (GDL) to assess their efficacy in producing H_2O_2 in a 0.5 M NaCl solution. The results demonstrated that a catalyst with the P-C structure efficiently performed in terms of the 2e⁻ ORR and anti-chlorine activity in the NaCl solution. According to the DFT calculations, when Cl⁻ was present in the electrolyte, Cl⁻ preferentially bound to the P site. O_2 was then reduced to H_2O_2 in the 2e⁻ pathway due to the combined action of the adsorbed P site and the nearby C site. This structure had a much lower energy barrier for *O_2 than N-doped carbon materials. We used this electrode to create H_2O_2 in actual seawater and examined its effectiveness at deactivating marine microbes to demonstrate the viability of the P-C bond structure (Chlorella vulgaris). Our study could serve as a reference for the development of electrocatalyst designs for use in Cl⁻-bearing electrolytes and provide significant practical implications for the reduction of marine pollution.

2. Experimental methods

2.1. Chemicals and reagents

Ethylenediaminetetrakisphosphate (EDTMPA, $C_6H_{20}N_2O_{12}P_4$, 98%), nitric acid (HNO_3, 65%−68%), cerium(IV) sulphate (Ce(SO₄)₂·4 H_2O, AR), hydrogen peroxide (H_2O_2, 30%), 5% Nafion solution, isopropanol (C_3H_8O, AR), fresh seawater (from Yellow Sea waters, 121° 54′ E, 38° 86′ N, pH ~ 7.8), sodium chloride (NaCl, AR), sodium hydroxide (NaOH, AR), sodium perchlorate (NaClO₄, AR), sodium carbonate (Na₂CO₃, AR), sodium nitrate (NaNO₃, AR), potassium dihydrogen phosphate (KH₂PO₄, AR), urea (CH₄N₂O, AR), fluorescein diacetate (FDA, $C_{24}H_{16}O_7$, AR), Propidium iodide (PI, $C_{27}H_{34}N_4I_2$, AR).

2.2. Characterization

The powder X-ray diffraction (XRD) experiment was tested by Shimadzu XRD-6100. The 2θ range was 10° ∼ 70° with a scanning step of 8° min⁻¹ (40 kV, 40 mA, Cu target). Laser Confocal Raman Spectroscopy (Raman) was tested by Thermo Fisher Dxr2xi. The Field Emission Scanning Electron Microscopy (FE-SEM) tests used SUPRA 55 SAPPHIRE (ZEISS) under a working voltage of 3 kV. Both transmission electron microscope (TEM) and EDS tests used FEI Talos F200S Super-X. The X-ray photoelectron spectroscopy (XPS) was tested with Thermo Fisher Scientific k-alpha. The charge correction was carried out with C 1 s = 284.8 eV binding energy as the energy standard. Electrochemical measurements were tested with dual potentiostat (CORREST, CS2150H) and RRDE-1A (DEYI, Shandong). Fourier Transform Infrared Spectroscope (FT-IR) was analyzed by Thermo Fisher Nicolet Is10.

2.3. Synthesis of catalysts

2 g of EDTMPA was spread evenly and flatly in a ceramic crucible and heated to different temperatures (600 °C ∼ 900 °C) in an H_2/Ar (5% H_2 v/v) atmosphere at a temperature-increasing rate of 4.7 °C min⁻¹ and held for 6 h. The resulting black solid was thoroughly ground and acid-washed using a concentration of 0.5 M HNO_3 for 8 h to remove impurities (at room temperature). Deionized water was used to wash the sediments until the remaining waste solution reached a neutral pH. The solids were vacuum dried at 50 °C for 12 h, cooled to room temperature, and grinding. The samples were named E600, E700, E800, and E900, depending on the carbonation temperature.

2.4. Electrochemical characterization

To investigate the number of electron transfers and the selectivity for H_2O_2 of different samples, electrocatalytic ORR performance tests were carried out in a three-electrode system using a rotating ring-disk electrode (RRDE) as the working electrode (WE), an Ag/AgCl electrode as the reference electrode (RE) and a Pt sheet as the counter electrode (CE). The electrolytes used were 0.5 M NaCl (pH=7) and 0.5 M NaCl + 0.1 M NaOH (pH=13). The electrocatalyst ink solution was first prepared by taking 5 mg of the catalyst, adding 950 μl of isopropanol (IPA) and 50 μl of Nafion solution (DuPont, D520, 5%), and sonicating for 20 min to mix thoroughly. The electrolyte was pre-saturated with O_2 for 30 min before the test, and O_2 was introduced continuously during the test. For the ORR test, the disk electrode was tested at a potential range of 0–1 V vs. RHE with a sweep rate of 10 mV s⁻¹ and a constant potential applied to the ring electrode of 1.26 V vs. RHE. The RRDE was tested at a rotation speed of 1600 rpm. The disk current for the ORR was obtained by subtracting the corresponding background current (the background current was obtained by testing at N_2 saturation under the same conditions). The equations for the H_2O_2 selectivity and the number of electrons transferred (n) were estimated by Eqs. (1) and (2) [27,28]:

$$H_2O_2(\%) = \frac{200 \times I_{ring}/N}{|I_{disk}| + I_{ring}/N} \qquad (1)$$

$$n = \frac{4|I_{disk}|}{|I_{disk}| + I_{ring}/N} \qquad (2)$$

where I_{disk} and I_{ring} are the disk and ring currents respectively and N is the collection factor of the Pt ring (N = 0.37). The equation for converting the potential relative to Ag/AgCl to the reversible hydrogen electrode (RHE) potential was eliminated by Eq. (3):

$$E_{RHE} = E_{Ag/AgCl} + 0.0591 \times pH + 0.197 \qquad (3)$$

The cyclic voltammetry (CV) and linear scanning voltammetry (LSV) tests were carried out in an O_2-saturated and N_2-saturated environment respectively, both in the same potential range as the ORR test, with a

sweep rate of 20 mV s^{-1} and an electrode speed of 0 rpm for the CV test, 10 mV s^{-1} and rotation speeds of 400, 900, 1600 and 2500 rpm for the LSV test. The Tafel slope was used to characterize the reaction rate of the catalyst and the speed control step of the electrode reaction. The Tafel slope was calculated from the Tafel equation, which is shown in Eq. (4) [29]:

$$\eta = a + b\log|j| \tag{4}$$

where η is the overpotential, a and b are constants and j is the kinetic current density in mA cm^{-2}. The electrocatalytic active surface area (ECSA) test is used to investigate the active surface area of the catalyst and CV tests are carried out in a nitrogen saturated electrolyte. The potential range tested is 1.05 ~ 1.15 V vs. RHE with sweep rates of 10, 20, 40, 80 and 120 mV s^{-1}.

2.5. H$_2$O$_2$ production by electrocatalytic ORR

For the electrocatalytic H$_2$O$_2$ production experiments, a self-developed and assembled flow-cell reactor was used (Supplementary Data, Fig. S1). The reactor has a reaction area of 4 cm^2 and a volume of 4 cm^3 on both sides of the reaction chamber, separated by a proton exchange membrane (PEM, Nafion 117, DuPont). A gas flow path is designed at the cathode to improve the contact between the gas and the electrode, and an Ag/AgCl electrode can be inserted in the cathode chamber to enable flow-cell testing of the three-electrode system.

In this experiment, carbon paper (Sigracet 39BB) containing a gas diffusion layer was used as a substrate for the preparation of the cathode electrode. The catalyst was uniformly coated onto the surface of the carbon paper with a loading of 0.5 mg cm^{-2}, dried at 50 °C and then clamped at the cathode reaction chamber for reactor assembly using high purity Ti flakes as the conductive medium, and the anode was a high purity Pt flake electrode (99.99%). The cathode and anode chambers were each connected to a peristaltic pump and reservoir with a flow rate of 80 mL min^{-1} and a volume of 50 mL of electrolyte solution used for each reaction. the gas flow path on the outside of the cathode was continuously fed with O$_2$ during the test at a rate of 10 L min^{-1}. the duration of the test was 20 min and a certain volume of cathode electrolyte was taken at the end of the test for quantitative testing.

In this work, the H$_2$O$_2$ was quantified using the cerium measurement method [8,30,31] and the equation for the reaction between Ce^{4+} and H$_2$O$_2$ is shown as Eq. (5):

$$H_2O_2 + 2Ce^{4+} + 2H^+ \rightarrow 2Ce^{3+} + 2H_2O \tag{5}$$
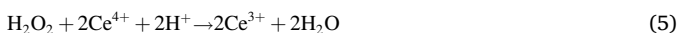
A 1 µM Ce(SO$_4$)$_2$ solution was prepared, mixed by adding different volumes of a 0.1 wt% H$_2$O$_2$ solution, and the absorbance at 318 nm was measured using a UV spectrophotometer to determine the relationship between the concentration of Ce^{4+} and absorbance, which was then converted to the relationship between the concentration of H$_2$O$_2$ and absorbance and fitted to a straight line graph as shown in Fig. S2. After the reaction, a certain volume of cathodic electrolyte was added to the Ce(SO$_4$)$_2$ solution, mixed well, and its absorbance at 318 nm was measured again. The absorbance results obtained from the test were substituted into the fitting equation to calculate the concentration of Ce^{4+} and then into the following conversion Eq. (6):

$$H_2O_2 \text{ concentration} = \frac{C_0 \times V_0 - C_1 \times V_1}{2 \times V_{tot.}} \tag{6}$$

where C_0 is the Ce^{4+} concentration of the original Ce(SO$_4$)$_2$ solution, V_0 is the volume of the original Ce(SO$_4$)$_2$ solution used, C_1 is the Ce^{4+} concentration of the solution after the color development reaction, V_1 is the sum of V_0 and the additional volume of liquid to be added, and $V_{tot.}$ is the total volume of the cathode electrolyte.

The Faradaic efficiency of H$_2$O$_2$ production is calculated using the Faraday equation as Eq. (7) [32]:

$$\text{Faradaic Efficiency (\%)} = \frac{2C \times V_{tot.} \times F}{Q} \times 100\% \tag{7}$$

where 2 is the number of electrons transferred for the reduction of O$_2$ to produce H$_2$O$_2$, C is the concentration of H$_2$O$_2$ (mol L^{-1}), $V_{tot.}$ is the volume of electrolyte (L); F is Faradaic constant, equal to 96,485.3 C mol^{-1}, and Q is the amount of electricity transferred during the reaction (Q).

The procedure for the cycle stability test was the same as described above for the electrocatalytic H$_2$O$_2$ production experiments, set for one cycle of 20 min, without replacing the carbon paper electrodes. Only the electrolyte in the cathode reservoir and anode reservoir was replaced, and a certain volume of electrolyte was added to the Ce(SO$_4$)$_2$ solution at the end of the test for quantitative testing.

2.6. Inactivation of Chlorella vulgaris by flow-cell reactor

Chlorella vulgaris was used as the inactivation target, and commercial seawater chlorella species were inoculated into seawater medium. Firstly, the seawater medium was made by filtering fresh seawater with a 0.22 nm micron pore size membrane to remove impurities. The filtered seawater was then sterilized in an autoclave held at 120 °C for 20 min, and then added 0.02 g L^{-1} Na$_2$CO$_3$, 2 g L^{-1} NaNO$_3$, 0.02 g L^{-1} KH$_2$PO$_4$, and 0.8 g L^{-1} urea after the seawater had cooled to room temperature. Then, the seawater was inoculated with Chlorella at a concentration of 1.75×10^8 cells L^{-1}. After inoculation, the solution is placed in a light incubator and incubated at 25 °C in a constant temperature shaker, alternating between light and dark for 12 h each. The propagated Chlorella solution was diluted to a concentration of 1×10^5 cells L^{-1} using filtered fresh seawater. 50 mL was taken into the cathode reservoir of the flow-cell reactor and cycled at a set constant current, with 3 mL sampled at different time points. 3 mL of the untreated diluted Chlorella solution was centrifuged as a control sample.

Observation of Chlorella survival using fluorescent staining [33–35]. The algal solution was centrifuged at 3000 r min^{-1} for 5 min and the supernatant was removed and washed once with deionized water. The supernatant was washed once, and the FDA and PI staining solutions were added separately. They were mixed well and left to stand for 5 min in a place protected from light. After centrifugation, the supernatant was added to deionized water and centrifuged three times. The last time, it was diluted to 3 mL with Dulbecco's phosphate buffered saline (Solarbio). A certain amount of the stained algal solution was pipetted onto a hematocrit plate. The cells were observed under a fluorescent microscope at a magnification of 40 × .

2.7. Theoretical study

The CASTEP package calculation model was used to calculate the O$_2$/Cl$^-$ adsorption energy and the Dmol3 package was used to calculate the free energy of the 2e$^-$ ORR process [36–38]. The exchange-correlation energy function is described by the generalized gradient approximation of the Perdew-Burke-Ernzerhof (GGA-PBE) function, and the convergence criterion per atom is set to a residual energy of 1×10^5 eV and a force of 0.005 eV Å^{-1}. In the CASTEP calculations, the kinetic cut-off energy of the plane wave is set to 435 eV. Using a $5 \times 5 \times 1$ graphene supercell as a simulation model, with a vacuum layer thickness of 20 Å and *k*-points in the Brillouin zone sampled by a $3 \times 3 \times 1$ grid, the adsorption energy is calculated as Eq. (8) [39]:

$$E_{ads.} = E_{tot.} - E_{catal.} - E_x \tag{8}$$

where E_{total} is the total cell energy of the catalyst after adsorption of O$_2$ or Cl$^-$, $E_{catal.}$ is the total catalyst energy and E_x is the energy of O$_2$ or Cl$^-$.

Dmol3 calculations were also performed using a $5 \times 5 \times 1$ graphene supercell used as a simulation model with a vacuum layer thickness of

20 Å. The computational hydrogen electrode (CHE) model was used to calculate the Gibbs reaction free energy change (DG) for each step in the 2e⁻ ORR, and according to the CHE model, DG values were calculated as Eq. (9) [40]:

$$\Delta G = \Delta E_{DFT} + \Delta E_{ZPE} - T\Delta S \tag{9}$$

where ΔE_{DFT} is reaction energy, ΔE_{ZPE} is zero-point energy, and is entropy at T = 298.15 K. For the 2e⁻ ORR, the two-step reaction is as Eqs.
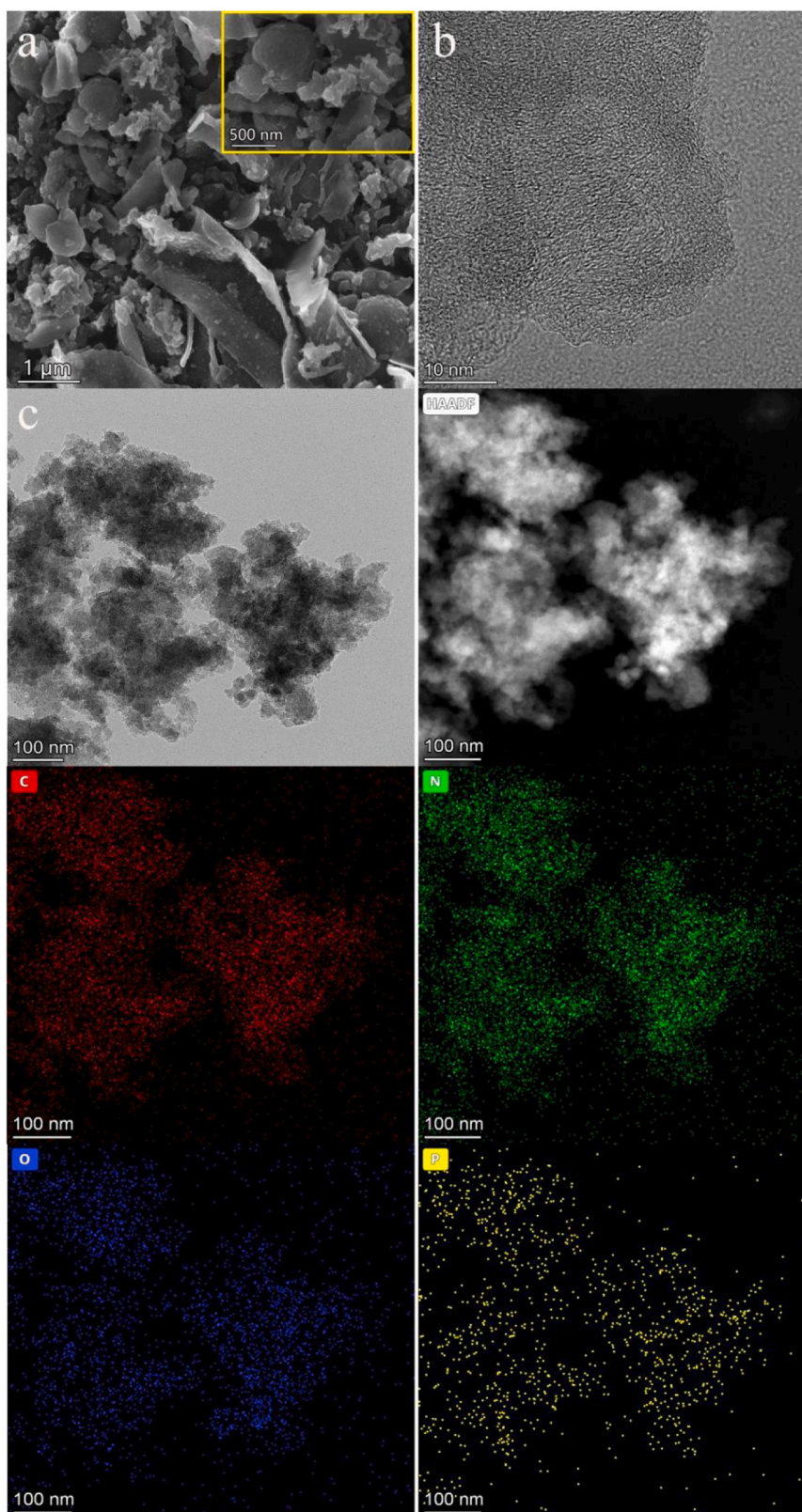

Fig. 1. (a) FE-SEM image, (b) HRTEM image, (c) HAADF TEM images and elemental mapping images of E700.

(10) and (11):

$$*O_2 + H^+ + e^- \rightarrow *OOH \qquad (10)$$

$$*OOH + H^+ + e^- \rightarrow *H_2O_2 \qquad (11)$$

Under standard conditions (298.15 K, 1 atm., pH = 0), the free energy of $(H^+ + e^-)$ is equal to the free energy of $1/2 H_2$.

3. Results and discussion

3.1. Structure and composition characterization

Ethylenediamine tetra(methylene phosphonic acid) (EDTMPA) is a low-cost chelating agent and inherently rich in P elements and can form P doped carbon-based catalysts after high-temperature carbonization; these catalysts are used in the preparation of substrates for electrocatalysts [41–43]. To investigate the effect of different temperatures on the microstructure of EDTMPA after carbonization, the samples were tested via X-ray diffraction (XRD) and Raman spectroscopy. As shown in Fig. S3a, the samples carbonized at different temperatures showed broad peaks near the diffraction angles of 26° and 43°, reflecting a classical planar structure of graphitic carbon and indicating that EDTMPA formed an amorphous carbon structure in the temperature interval of 600–900 °C [44]. In particular, as the carbonization temperature increased, the diffraction peak at approximately 26° was slightly shifted to a lower angle, indicating a larger crystal spacing of the graphitic

lattice layer structure [45]. We speculated that since P self-doping occurred in EDTMPA during the carbonization process, the P atoms entered into the interior of the graphite-carbon lattice as the temperature increased; since the atomic diameter of P (0.206 nm) was larger than that of C (0.182 nm), the graphite lattice layer spacing increased. The curved lattice stripes (indicated amorphous carbon structure) were also observed in the transmission electron microscopy (TEM) images of the E700 sample, the sample was a mixture of irregular block and lamellar morphology, and the uniform distribution of C, N, O, and P elements was observed in the TEM mapping (Fig. 1). The morphology of the samples carbonized at other temperatures did not significantly change (Figs. S4–7).

In the Raman spectrum (Fig. S3b), the I_D/I_G reflected the degree of defects and ordering of the crystal structure of the samples. The D and G peaks appeared at 1330 cm^{-1} and 1585 cm^{-1} for all four samples, respectively; The value of I_D/I_G increased from 0.958 to 1.009 with increasing temperature, indicating that the defect content of the samples increased with increasing temperature and that the graphite structure ordering increased with increasing temperature [46,47]. This phenomenon corresponded to the (0 0 2) peak shift in the XRD data because the mismatch of atomic radii led to the generation of more defects inside the graphite lattice as the P self-doping further deepened.

The X-ray photoemission spectroscopy (XPS) data showed the structural information of the different elements in the sample (as shown in Table S1). With increasing carbonization temperature, the contents of O, N and P in the sample decreased, while the content of C increased.
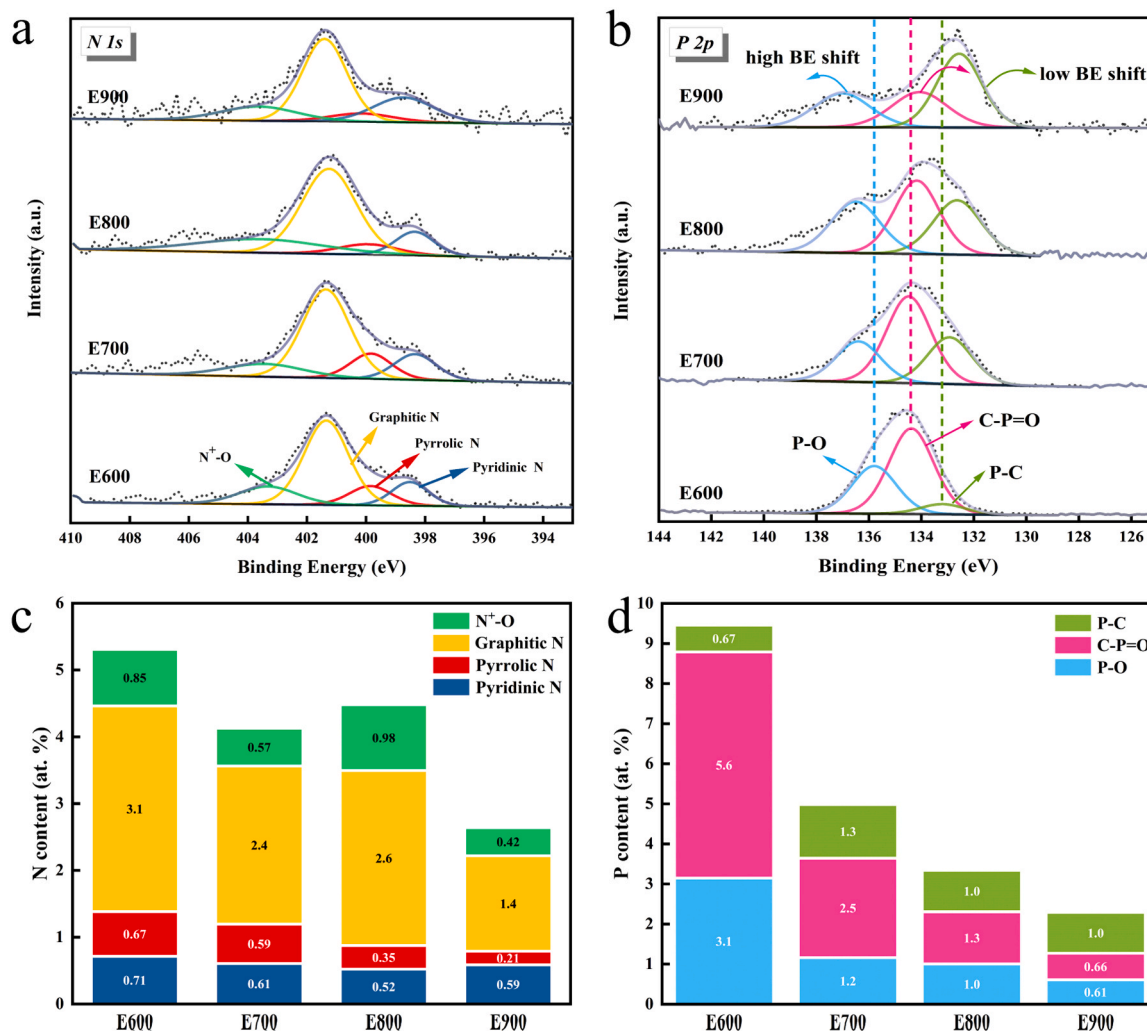

Fig. 2. High-resolution XPS spectrum of (a) N 1 s, (b) P 2p for E600, E700, E800 and E900. Proportion of (c) N 1 s, and (d) P 2p bonding types.

Tables S2-S5 presents the changes in binding energy for C 1 s, O 1 s, N 1 s, and P 2p, respectively. The high-resolution XPS spectrum of C 1 s, depicting the distribution of bond structures, were shown in Fig. S8(a) (c). Across all samples, the C 1 s spectrum exhibited similar binding energy positions, with an increasing peak area of the anti-convolution peak as the carbonization temperature rises [48]. Fig. S8(b)(d) illustrated the variations in O 1 s. The binding energy of the C=O bond remained consistent among all samples, while the binding energy of the C-O/P-O and C-OH bonds remained nearly constant within the range of 600–800 ℃ [49]. However, a positive shift in the binding energy of C-O/P-O and C-OH was observed at 900 ℃, indicating an increase in the bond length of C-O at high temperatures. Four different forms of N were shown in the N 1 s orbital high-resolution pattern (Fig. 2a): graphitic N (401.3 eV), pyridinic N (398.3 eV), pyrrolic N (399.8 eV), and N^+-O (403.4 eV) [45]. In the structural scale diagram of these structures (Fig. 2c), graphitic N was the main form of N present in the sample, and the remaining three forms were less than 1% in the sample. In addition, the content of both pyrrolic N and pyridinic N showed a decreasing trend with increasing carbonization temperature, which was caused by the increase in the graphite structure with increasing carbonization temperature and its ordering [50]. The high-resolution XPS spectrum of the P 2p orbital (Fig. 2b) revealed the presence of the P element in three forms: P-O, C-P = O, and P-C bonds[51–54]. The ratios of these forms are illustrated in Fig. 2d. Notably, the variations in P 2p during the self-doping process show a significant correlation with the carbonization temperature. At lower carbonization temperatures, the dominant forms of P elements in the samples are P-O and C-P = O bonds. As the temperature increases, the proportion of P-C bonds increases, while the proportion of P-O and C-P = O bonds decreases. The P-O characteristic peak undergoes a positive shift towards higher binding energy (from 135.7 eV to 137.1 eV), while the C-P = O peak experiences a slight shift towards lower binding energy (from 134.3 eV to 134.1 eV), and the P-C bond shifts towards lower binding energy (from 133.2 eV to 132.5 eV). It is speculated that the combination of high temperature and a reducing atmosphere leads to the cleavage of P-O bonds, resulting in the loss of P elements. These results indicated that the carbonation temperature determined the direction of electron migration from the unstable P-O bond structure to the stable P-C bond structure [53]. The findings from XRD and Raman spectrum also support this speculation, demonstrating that adjusting the carbonization temperature can modify the electronic structure of the sample.

Additionally, the samples were subjected to FT-IR spectrum analysis to characterize their chemical bond structures and functional groups (Fig. S9). The wave number range of 1030 ~ 1336 cm^{-1} exhibited a broad peak corresponding to the characteristic absorption of C-N stretching vibration[51,55]. For E600, two distinct peaks in the range of 1000 ~ 1200 cm^{-1} were observed, representing the P-O (1036 cm^{-1}) and P = O structures in the phosphate group[56,57]. Additionally, a weaker peak indicating the P-C stretching vibration in the aromatic structure was present at 1120 ~ 1130 cm^{-1} [58]. This peak became more prominent with increasing pyrolysis temperature. Furthermore, the characteristic peaks of P = O and P-O gradually diminished and disappeared at 900 ℃. This finding aligned with the XPS test results, where the shift of the P-O bond towards higher binding energy corresponds to the movement of the P-C bond towards lower binding energy. This suggested that phosphorus atoms become more stabilized within the carbon conjugate ring, which correlated with the increased graphite ordering observed in the Raman spectrum. Moreover, all samples exhibited a weak peak indicating the stretching vibration of the C=O bond at 1797 cm^{-1}. This suggests that oxygen atoms may form carbonyl groups with carbon atoms during the pyrolysis of EDTMPA at 600 ~ 900 ℃[59,60].

3.2. ORR performance

In our study, a three-electrode system was used to evaluate the ORR

performance of the catalyst. Since a flow-cell reactor with a PEM was used, the cathode chamber accumulated a large amount of OH^- as the reaction continued, resulting an alkaline environment; thus, to fit the actual reaction environment of the catalyst, the electrocatalytic performance of the catalyst in the neutral environment containing chlorine (0.5 M NaCl) and the alkaline environment (0.1 M NaOH + 0.5 M NaCl) was evaluated. Cyclic voltammetry (CV) tests were performed under N_2-saturated and O_2-saturated conditions (Fig. S10); the samples obtained by carbonization at different temperatures showed strong oxidation peaks under O_2-saturated conditions, while no oxidation peaks were found under N_2-saturated conditions, indicating that all four samples had good oxygen reduction activity in both neutral and alkaline Cl^- bearing electrolytes. Subsequently, to evaluate the catalyst selectivity for the $2e^-$ ORR, a rotating ring-disk electrode (RRDE) was used to evaluate that the catalyst loaded on a glassy carbon disc electrode polarized at different potentials; its generated H_2O_2 was oxidized to H_2O by a Pt ring electrode loaded with a certain potential to generate a current [61].

The RRDE test results are shown in Fig. 3**a** and **c**, and under neutral conditions, the H_2O_2 selectivity of the samples with electron transfer number decreased with a negative shift of potential (Fig. 3**b**), while the sample was more stable under alkaline conditions (Fig. 3**d**). Furthermore, the ORR performance of the samples under alkaline conditions was better than that under neutral conditions. The H_2O_2 selectivity and the number of transferred electrons of the E700 sample were better than those of the other samples in both neutral and alkaline environments. In a neutral environment, at a potential of 0.45 V vs. RHE, the H_2O_2 selectivity of E700 was 85.10%, and the number of transferred electrons was 2.29; in an alkaline environment with different potentials, the H_2O_2 selectivity ranged from 80.13% to 82.86%, and the electron transfer number ranged from 2.34 to 2.40. With increasing carbonization temperature, the disk current density of the samples significantly increased, but the ring current weakened, indicating that the $2e^-$ ORR performance of the samples worsened with increasing carbonization temperature (see Tables S6–7). The reason for this phenomenon was caused by both the decrease in the pyrrolic N/pyridinic N ratio and the decrease in the P-C structure due to the increase in the carbonization temperature [62]; moreover, the samples had more π-π structures with increasing carbonization temperature (Fig. S8), and the electron-rich π-π structures could significantly promote the interaction between O_2 and the catalyst surface and enhance the $4e^-$ ORR performance, which can decrease the $2e^-$ ORR performance[63,64]. In contrast, in the sample carbonized at low temperature (E600), although its $2e^-$ ORR performance was better than that of the sample carbonized at high temperature (E800, E900), it also decayed compared to E700, and the pyrrolic N/pyridinic N ratios of E600 and E700 were similar; thus, this could be potentially related to the P-C bond structural content of the sample, which is analyzed in detail later in the calculation section.

The onset potential E_{onset} (potential at a current density of 0.1 mA cm^{-2}) and half-wave potential $E_{1/2}$ (measured at the limit diffusion current density 1/2) were analyzed for different samples (Table S8), and the E_{onset} and $E_{1/2}$ reflect the intrinsic and catalytic activity of the catalyst ORR, respectively. The E_{onset} and $E_{1/2}$ of the samples increased with increasing temperature, which was attributed to the gain effect of the elevated graphitization on the $4e^-$ ORR activity induced by the high-temperature carbonization [65,66]. This is different from the results of RRDE test, which shows that the E_{onset} and $E_{1/2}$ are not decisive factors for evaluating the $2e^-$ ORR activity. The ORR kinetic performance of the samples was further quantified by fitting Tafel curves, and the results of the Tafel slope (Fig. 4a-b, Figs. S11 and 12, Table S8) also indicated that the ORR kinetics of E700 were optimal under either neutral or alkaline conditions. Electrochemical surface area (ECSA) is commonly used for bilayer capacitance measurements of carbon-based catalysts to determine the electrocatalytic active area of the catalyst. The ECSA test results for the four samples showed (Fig. 4c-d, Figs. S13 and 14, Table S8) that the electrocatalytically active
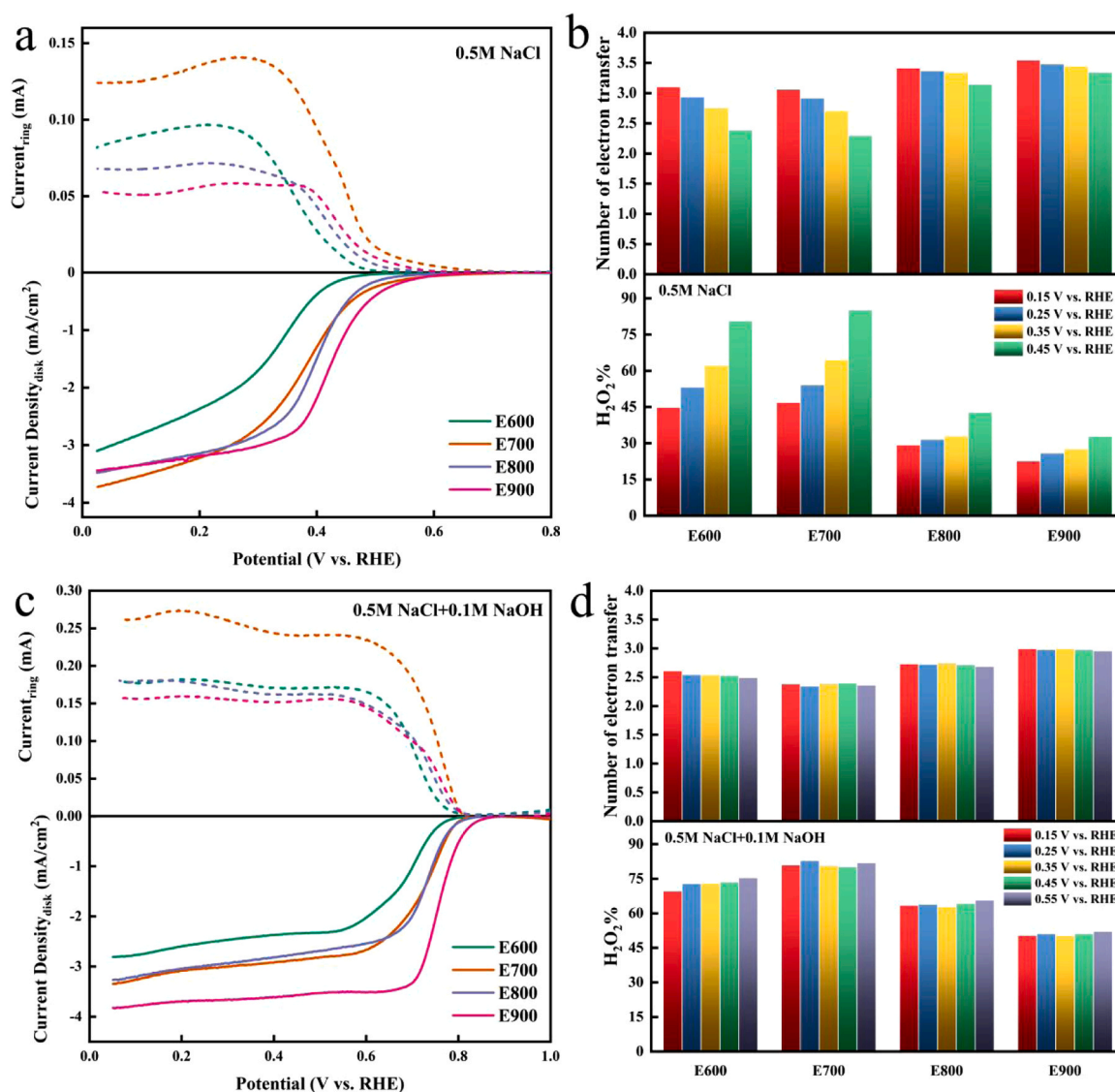
Fig. 3. RRDE test for E600, E700, E800, and E900 with a rotation rate of 1600 rpm in O_2-saturated (a) 0.5 M NaCl and (c) 0.5 M NaCl + 0.1 M NaOH (ring current was corrected by N). The number of electron transfer and H_2O_2 selectivity for E600, E700, E800 and E900 in O_2-saturated (b) 0.5 M NaCl and (d) 0.5 M NaCl + 0.1 M NaOH.

area of the samples increased with increasing carbonization temperature, which was also consistent with the trend of increasing disk current density with increasing carbonization temperature in RRDE but different from the trend of 2e⁻ ORR performance. Interestingly, several studies have shown that the decrease in catalyst ECSA accelerated the formation of H_2O_2 during the ORR reaction [67,68], and although the increase in carbonation temperature exposed more active sites in the material, it also promoted the further reaction of O_2 into water, which led to a decrease in 2e⁻ ORR selectivity. The experimental results showed that E700 had the best 2e⁻ ORR activity among these samples under chlorine-containing electrolyte conditions, and the increase in temperature at a sample carbonization temperature above 700 °C led to a decrease in the 2e⁻ ORR performance of the samples. First, the percentage of pyrrolic N in the 2e⁻ ORR active site decreased and the percentage of pyridinic N in the 4e⁻ ORR active site increased, while the high carbonization temperature caused the catalyst to expose more 4e⁻ active sites (rise of ECSA), enabling further dissociation of *OOH and a decrease in 2e⁻ ORR selectivity. At temperatures below 700 °C, the lack of carbonation led to a lower proportion of the P-C bond structure, the P-O and C-P = O bond structures were the main form of P in E600, and the ORR activity at the P-O site was lower than its activity at the P-C site.

Additionally, the C-P = O structure cannot serve as an active site for ORR due to its saturated electronic configuration, which hinders oxygen adsorption. The relationship between the P-O site and the ORR selectivity is further analyzed in the calculation section.

The results of several studies have shown that the presence of Cl⁻ had a toxic effect on the ORR catalyst [11]; therefore, to verify the interaction of Cl⁻ with the catalyst surface during the ORR, the H_2O_2 selectivity of E700 was tested in 0.5 M NaClO₄ (pH=7) vs. 0.1 M NaOH (pH=13), respectively. Under neutral conditions (Fig. 5a), the H_2O_2 selectivity of E700 in 0.5 M NaCl was superior to that in 0.5 M NaClO₄ (0.45 V vs. RHE, 85.11% in 0.5 M NaCl, 74.03% in 0.5 M NaClO₄), with the same trend under alkaline conditions (Fig. 5b) (0.45 V vs. 80.14% in 0.5 M NaCl, 50% in 0.1 M NaOH + 0.5 M NaCl). In the Cl⁻-containing environment, there was a slight decrease in the ring current density of the catalyst, but there was a significant increase in its ring current magnitude. This was potentially due to the presence of Cl⁻ affecting the electronic environment on the catalyst surface, enhancing its selectivity for the 2e⁻ ORR path, and thus improving the ORR performance of the catalyst in the Cl⁻-containing environment.

Considering the interference of oxygen-containing functional groups on the results of ORR tests, the E700 sample was reduced to eliminate
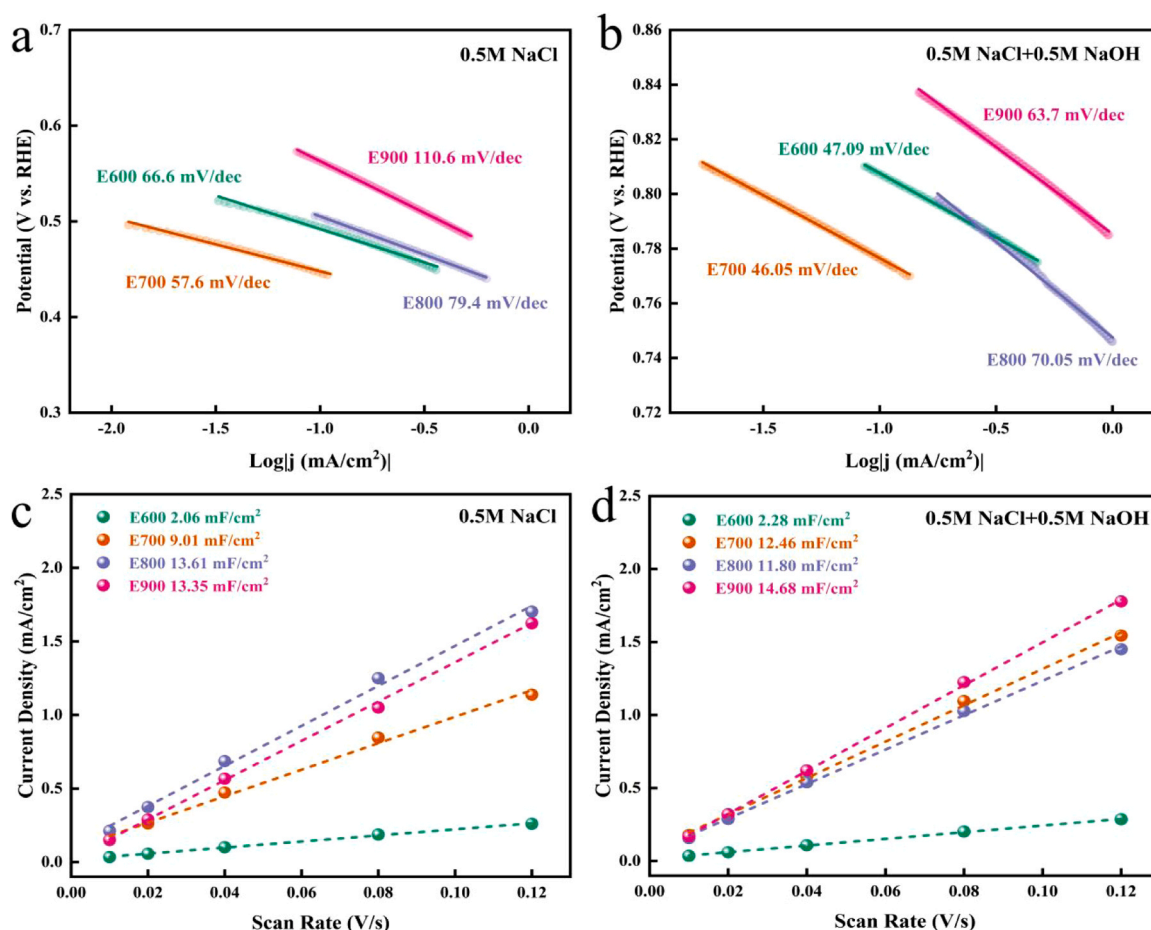
Fig. 4. Tafel slope of E600, E700, E800 and E900 in (a) 0.5 M NaCl and (c) 0.5 M NaCl + 0.1 M NaOH. ECSA of E600, E700, E800 and E900 in (b) 0.5 M NaCl and (d) 0.5 M NaCl + 0.1 M NaOH.
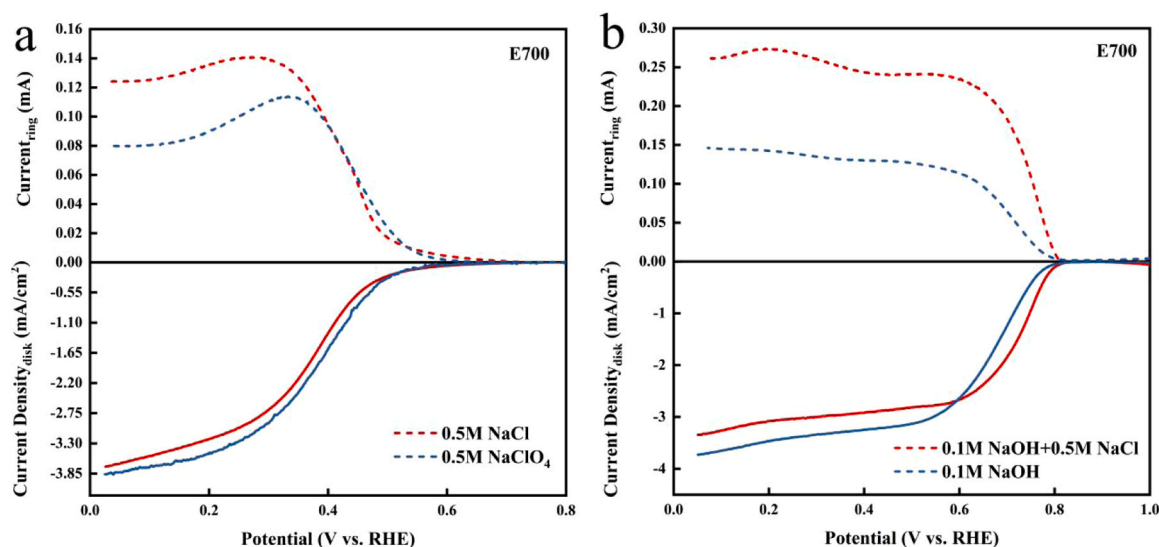

Fig. 5. RRDE test for E700 with a rotation rate of 1600 rpm in O_2-saturated (a) 0.5 M NaCl, 0.5 M $NaClO_4$ and (b) 0.1 M NaOH + 0.5 M NaCl, 0.1 M NaOH.

the influence of surface oxygen-containing functional groups on the outcomes. The preparation method for the reduced sample (R-E700) was provided in supporting information. Subsequently, XPS characterization was performed on the reduced sample, and the elemental contents before and after the reduction treatment are presented in Table S9. The

oxygen content only decreased by 2.75%, the nitrogen content decreased by 0.7%, the carbon content increased by 3.03%, and the P content remained nearly unchanged. Notably, the most significant change observed in the XPS high-resolution spectrum, as depicted in Figs. S15 and 16 and Tables S10-S13, was the decrease in C═O content

from 6.9% to 4.0%. Additionally, the percentage of the P-O bond in P 2p decreased from 1.2% to 0.5%, while the percentage of the P-C bond increased from 1.3% to 2%. The observed shifts in binding energy clearly indicate that the electronic structure of oxygen underwent obvious changes during the reduction of E700, while the unreduced oxygen may exist in the carbon matrix. Subsequently, the samples were subjected to RRDE testing in both 0.5 M NaCl and 0.5 M NaClO$_4$, as illustrated in Fig. S17(a). The catalytic activity of the reduced sample decreased by about 0.1 V in the E$_{1/2}$ (0.533–0.423 V in 0.5 M NaCl, 0.515–0.416 V in 0.5 M NaClO$_4$). The results demonstrated an enhanced selectivity of the catalyst towards H$_2$O$_2$ at high potentials following the reduction of surface oxygen-containing functional groups, albeit with a negative shift in the ORR starting potential. Previous studies have indicated that the surface oxygen-containing functional groups (e.g. C=O) act as the active site for the 2e$^-$ ORR [48,69]. The negative shift in the E$_{1/2}$ may be attributed to the reduction in the number of active sites after eliminating the oxygen-containing functional groups. Conversely, the increased percentage of the P-C bond structure bolstered the selectivity towards H$_2$O$_2$, reaffirming the effectiveness of P-C bond structure as an excellent active site for the 2e$^-$ ORR. These findings support the notion that the P-C bond structure serves as an outstanding two-electron ORR active center in chloride-containing electrolytes.

To further substantiate the role of the P-C bond structure as 2e$^-$ ORR active sites in chlorine-containing electrolytes, we prepared a control sample (EDTA700) under identical conditions using a precursor EDTA with a similar structure. XPS characterization of EDTA700, as depicted in Fig. S18 and detailed in Tables S14–17, revealed similar bond structures to E700, with the exception of the absence of phosphorus elements. Subsequently, separate RRDE tests were conducted on EDTA700 in 0.5 M NaCl and 0.5 M NaClO$_4$, as illustrated in Fig. S17(b). Notably, the 2e$^-$ ORR selectivity of the EDTA700 sample was compromised in the presence of Cl$^-$ (64.11% in 0.5 M NaClO$_4$ and 56.05% in 0.5 M NaCl at 0.45 V). The reduction in selectivity can be attributed to the absence of the P-C bond structure in EDTA700, along with the significant presence of pyrrolic N and pyridinic N. The aforementioned experimental findings indicate that the P-C bond structure plays a crucial role in promoting the selectivity of the 2e$^-$ ORR path as the active site in Cl$^-$-bearing environments.

Furthermore, to inspect the potential interaction between the sample surface and Cl$^-$ during the electrocatalytic reaction, XPS analysis of the E700 electrode was conducted after testing at different potentials. The results are presented in Fig. S19. The CP blank refers to the carbon paper without electrocatalytic reaction, while the E700 blank represents the carbon paper loaded with E700 but without electrocatalytic reaction. In the presence of 0.5 M NaCl, as shown in Fig. S19(a)(b), the major peaks of C 1 s and N 1 s remained nearly unchanged on the E700 electrode after the reaction at different potentials, whereas significant changes were observed in the P 2p and Cl 2p orbitals. As depicted in Fig. S19c and detailed in Tables S18–21, the binding energy of the P-C bond experienced a substantial negative shift at the open circuit potential (E700 OCP), and then, the binding energies of P-C and C-P = O bonds exhibited a decreasing trend followed by an increasing trend with the negative shift of the applied potential. The changes in the Cl 2p orbitals are presented in Fig. S19(d) and Table S21, indicating the presence of two chloride structures: monovalent chloride ions in NaCl and chloride covalent bonds [70,71]. The behavior of these two structures mirrors that of P-C/C-P = O. It can be inferred that monovalent chloride ions and C-Cl bonds exist on the surface of the CP blank after reaction in NaCl solution. At the open circuit potential, both chloride ions and chloride covalent bonds on the E700 electrode surface displayed a negative shift compared to Cl species of the CP OCP. Based on these observations, it is speculated that chloride ions in the electrolyte can spontaneously interact with the phosphorus on the surface of the E700 electrode, and this interaction remains unaffected by the negative shift of the potential [72].

The catalyst needs to endure the high current operating conditions

and higher H$_2$O$_2$ yields if electrocatalytic production of H$_2$O$_2$ is to be industrialized. Mass transfer constraints caused by a limited oxygen solubility in conventional electrolytic cells could be overcome with the use of GDL electrodes [10]. To evaluate the development potential of the samples for industrialization, the 2e$^-$ ORR performance of E600, E700, E800 and E900 was tested using a three-electrode flow-cell reactor, and the H$_2$O$_2$ yields and Faradaic efficiencies were tested at current densities of 12.5, 25, 50, and 100 mA cm^{-2}. The results are shown in Fig. 6 and Table S22. All samples showed higher H$_2$O$_2$ yields at higher current densities, and the 2e$^-$ ORR was ranked as E700 > E600 > E800 > E900, which was consistent with the trend reflected by the electrocatalytic tests. E700 showed H$_2$O$_2$ yields of 0.37, 0.79, 1.69 and 3.33 mol g^{-1} h^{-1} at current densities of 12.5, 25, 50, and 100 mA cm^{-2}, respectively. The Faradaic efficiency tended to increase and then decrease with increasing current density, reaching a maximum of 92.10% at 50 mA cm^{-2} due to the occurrence of hydrogen evolution reaction (HER) at high current densities. Combined with the analysis from the material structural characterization test results, the P-C bond structure greatly contributed to the process of the 2e$^-$ ORR. P-doped carbon materials are generally believed to form sp^3 hybridization [24], and the P-C bond formed is longer than the C-C bond due to the larger radius of the P atom, which leads to distortion of the carbon structure; P doping leads to charge rearrangement of the material, and P functions as the active site for the 4e$^-$ ORR. However, our experimental results showed a significant difference. The results of the chlorine resistance tests showed that the P-C bond structure exhibited higher 2e$^-$ ORR activity in Cl$^-$-containing electrolytes, which is discussed in the subsequent DFT calculations.

To evaluate the stability of the catalyst in the simulated seawater environment, consecutive cycle stability tests were performed on the E700 sample (0.5 M NaCl), and the results are shown in Fig. S20. In the three-electrode flow-cell reactor, the yield of the E700 sample was maintained between 1.59 and 1.72 mol g^{-1} h^{-1} for each test, and the Faraday efficiency ranged from 86.09% to 93.18% without a significant decay trend. To investigate the effect of the cycle test on the sample structure, XPS analysis was conducted on the catalyst-loaded carbon paper electrode before and after the cycle. The XPS data (Figs. S21 and 22, Table S23) showed that the O content increased significantly before and after the cycle (Fig. S22b, d) due to the presence of a large amount of adsorbed O$_2$ on the surface of the carbon paper electrode after the reaction, which could form more C=O bonds. Tables S24-S27 presents the binding energy shifts observed in the XPS high-resolution spectrum of each element. Additionally, it was discovered that the binding energy of the bond structures for C 1 s and N 1 s experienced slight negative shifts, while the bond structure of P 2p exhibited a significantly negative shift. These shifts can be attributed to the interaction with Cl$^-$ present in the environment. Despite a slight decrease in N and P, the high-resolution orbital data of N 1 s (Fig. S21a, c) indicated a decrease in the content of pyrrolic N and pyridinic N in the sample, attributed to the increased N$^+$-O content resulting from the higher adsorbed O$_2$. However, the ratio of pyrrolic N to pyridinic N remained largely unchanged. Similarly to N 1 s, the high-resolution orbital data of P 2p (Fig. S21b, d) exhibited no alteration in the ratio of P-O to P-C bonds. In addition, the characteristic peaks of -CF$_2$-related groups appeared in the C 1 s high-resolution spectrum (Fig. S22a, c) [73,74] and were also found in the total spectrum (Fig. S22e) due to the addition of Nafion membrane solution during the fabrication of the electrode; the composition of the Nafion membrane solution changed as the electrocatalytic reaction proceeded, and the intensity of the -CF$_2$ characteristic peak changed before and after cycling. The appearance of the Na 1 s characteristic peak after cycling was caused by the adsorption of Na$^+$ in the NaCl solution by cycling. The results showed that the E700 sample was able to stably produce H$_2$O$_2$ in the simulated seawater environment.

Subsequently, to explore the potential of the flow-cell reactor for applications in marine environments, we replaced the electrolyte with real seawater containing a certain concentration of Chlorella and tested the performance of electrochemical synthesis of H$_2$O$_2$ for inactivation of
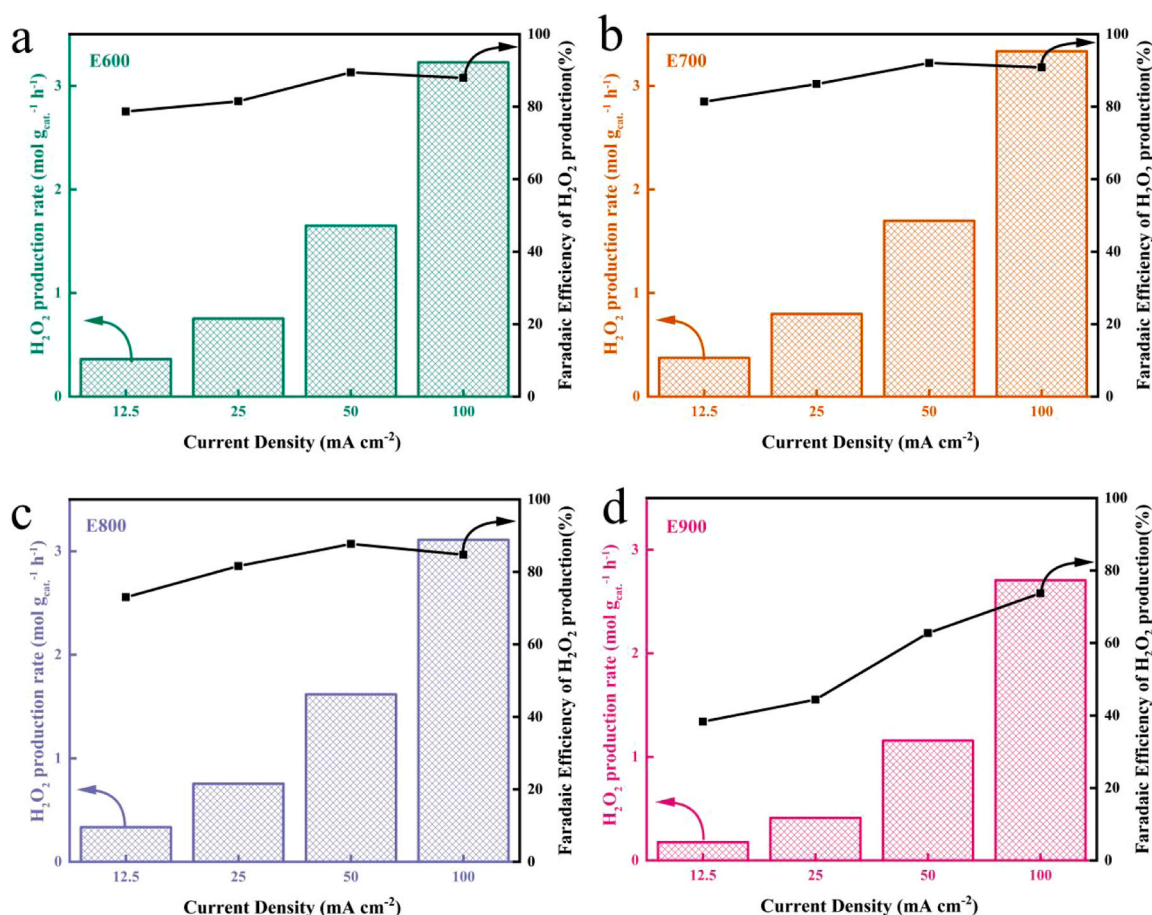
Fig. 6. Performance of H_2O_2 production rate and Faradaic efficiency in flow-cell in 0.5 M NaCl: (a) E600, (b) E700, (c) E800, (d) E900.

Chlorella using the E700 catalyst at a current density of 100 mA cm^{-2}. Conventional marine wastewater treatment (e.g., ballast water) uses a Fenton reaction with Fe^{2+}-containing reagents and UV light in combination with tedious steps [75,76]. In contrast, in our study, under the condition of no additional Fe^{2+} and UV light illumination, the seawater Chlorella was gradually deactivated with the extension of electrocatalytic treatment time, and the inactivation test results are shown in Fig. S23. Green fluorescence was observed under the fluorescence microscope (XSZ-N107CCD, YONGXIN OPTICS CO., LTD) for Chlorella cells without reactor treatment, and a small amount of deactivated Chlorella showed red color after 1 min (PI could penetrate the dead cell membrane and aggregate in the nucleus to emit red fluorescence); the number of cells showing red fluorescence increased significantly as the treatment time increased. At 10 min, almost all Chlorella fluoresced red in the field of view, indicating almost complete inactivation of Chlorella. After the reaction reached 20 min, the complete shape of Chlorella was not observed under the microscope (all were disrupted), and the field of view showed strong fluorescence. Since the principle of FDA staining was to react with esterases inside living cells to produce substances that could emit fluorescence, the cell structure of Chlorella was destroyed during the reactor treatment, and the fluorescent substances inside the cells spread to the external environment. The untreated Chlorella and the inactivated Chlorella after 20 min of treatment were fixed with glutaraldehyde solution and observed under FE-SEM, as shown in Fig. S24. The morphology of the inactivated Chlorella changed significantly, with the untreated Chlorella cells being distinct from each other and showing a bumpy texture on the surface, while the inactivated Chlorella cells adhered together and produced a smoother surface; this result indicated that the cell membranes were disrupted, which was consistent with the results of fluorescence bio microscopy. For the

inactivation experiments of Chlorella, the E700 catalyst could also maintain good electrocatalytic performance in real seawater solution, which was expected to provide H_2O_2 for the treatment of marine pollution via the Fenton reaction in seawater medium in the future.

3.3. The effect of P-C structure on ORR performance

To understand the reason for the promotion of the 2e$^-$ ORR performance of catalysts containing P-C bond structure by Cl$^-$-containing electrolytes, we performed DFT calculations. First, we compared the adsorption properties of O_2 and Cl$^-$ on the surfaces of graphitic N, pyridinic N, pyrrolic N, P-C, and P-O bond structures (see Figs. S25 and 26). The adsorption energies were as follows: -0.94 eV for O_2 and -1.59 eV for Cl$^-$ on P-C; -0.70 eV for O_2 and -2.81 eV for Cl$^-$ on P-O; -0.37 eV for O_2 and -0.24 eV for Cl$^-$ on graphitic N; -0.42 eV for O_2 and 0.38 eV for Cl$^-$ on pyridinic N, and -0.15 eV for O_2 and 0.37 eV for Cl$^-$ on pyrrolic N. The results of the adsorption energy calculations showed that graphitic N tended to adsorb O_2 when Cl$^-$ was present on the catalyst surface, and pyridinic N and pyrrolic N only adsorbed O_2, not Cl$^-$, which was consistent with the results reported in the literature showing that carbon-structured catalysts could maintain their 2e$^-$ ORR performance in Cl$^-$-containing electrolytes, while the P sites in the P-C and P-O bond structures were preferentially occupied by Cl$^-$. In addition, the C-P $=$ O bond structure (as depicted in Fig. S27) exhibits a positive adsorption energy for O_2, which indicates that C-P $=$ O bond structure cannot serve as an active site for ORR.

Based on the results of the Cl$^-$ adsorption energy calculations, we evaluated the free energy potentials of the different structures of the catalysts for the reaction intermediates. For graphitic N (Fig. S28), pyridinic N (Fig. S29) and pyrrolic N (Fig. S30) structures, *O$_2$

activation to *OOH was the rate-determining step (RDS) of the catalytic reaction, and the free energy potential barriers of graphitic N, pyridinic N and pyrrolic N for $*O_2$ activation to *OOH were 0.62 eV, 0.68 eV and 0.52 eV, respectively, at U= 0.7 V. This indicated that compared to graphitic N and pyrrolic N, the pyrrolic N structure had better 2e⁻ ORR performance. For the P-doped carbon materials, the P-O bond structure (Fig. S31) and the P-C bond structure (Fig. 7) exhibited differences in the 2e⁻ ORR performance. For the P-O bond structure, the P site did not act as an ORR site, the P occupied by Cl⁻ repelled the O_2 adsorption around it, and the ORR proceeded on the adjacent nitrogen site; the potential barrier for $*O_2$ activation to generate *OOH was lower than those of graphitic N and pyridinic N at U= 0.7 V and was determined to be 0.59 eV, indicating that the P-O bond structure reduced the O_2 activation potential barrier and promoted the 2e⁻ ORR to some extent. For the P-C bond structure with Cl⁻ adsorbed on the surface, $*O_2$ activation to generate *OOH was significantly enhanced. The results of some studies have shown that Cl⁻ pairs will hinder the adsorption of O_2 on the active site and thus led to a decrease in ORR activity. In our study, incredibly, when P was occupied by Cl⁻, O_2 molecules could still be adsorbed on the P-C bond by bridge adsorption, and this structure helped to enhance the activation of $*O_2$ by the catalyst. At U= 0.7 V, the free energy barrier of $*O_2$ to *OOH was only 0.19 eV, and this result showed that the P-C bond structure could significantly enhance the 2e⁻ ORR performance in the presence of Cl⁻. In addition, we also simulated the 2e⁻ ORR step on the catalyst surface after OH⁻ adsorption on the P site when the alkaline environment did not contain Cl⁻ (Fig. S32); when the P site was occupied by OH⁻, the ORR site shifted to the adjacent N site, and its free energy barrier for activation of $*O_2$ to generate *OOH was 0.58 eV at U = 0.7 V, indicating that OH⁻ occupation of the P site reduced the catalyst performance. This calculation was consistent with the ORR performance test results, where the potential barrier from $*O_2$ to *OOH significantly increased when the solution did not contain Cl⁻ and the pH was alkaline, thus reducing the 2e⁻ ORR performance. Finally, we also simulated the ORR process of O_2 on the surface of the P-C bond structure without Cl⁻ (Fig. S33); the results showed that *OOH could not be stabilized at the P site, and *OOH decomposed into *O and *OH, indicating that the 4e⁻ ORR path did occur in the P-C bond structure and confirming the promotion of Cl⁻ on the 2e⁻ ORR performance of the P-C bond structure from the side.

The results of DFT calculations indicated that the material containing the P-C bond structure could be an excellent performing catalyst for the 2e⁻ ORR in Cl⁻-containing electrolytes and could be a potential catalyst for the synthesis of H_2O_2 in seawater medium in the future. The 2e⁻ ORR process of the P-C bond structured catalyst in Cl⁻-containing electrolytes is shown in Fig. 8. In the presence of Cl⁻, the P-C bond structure significantly reduced the energy barrier of $*O_2$ to *OOH. Combining the catalyst performance test with the XPS results, the E700 catalyst containing the most P-C bond structure showed the optimal 2e⁻ ORR performance in Cl⁻-containing electrolytes, while E600 also exhibited good performance. As the carbonation temperature increased, the P content decreased significantly, and the 2e⁻ ORR performance of E800 and E900 showed a decreasing trend.
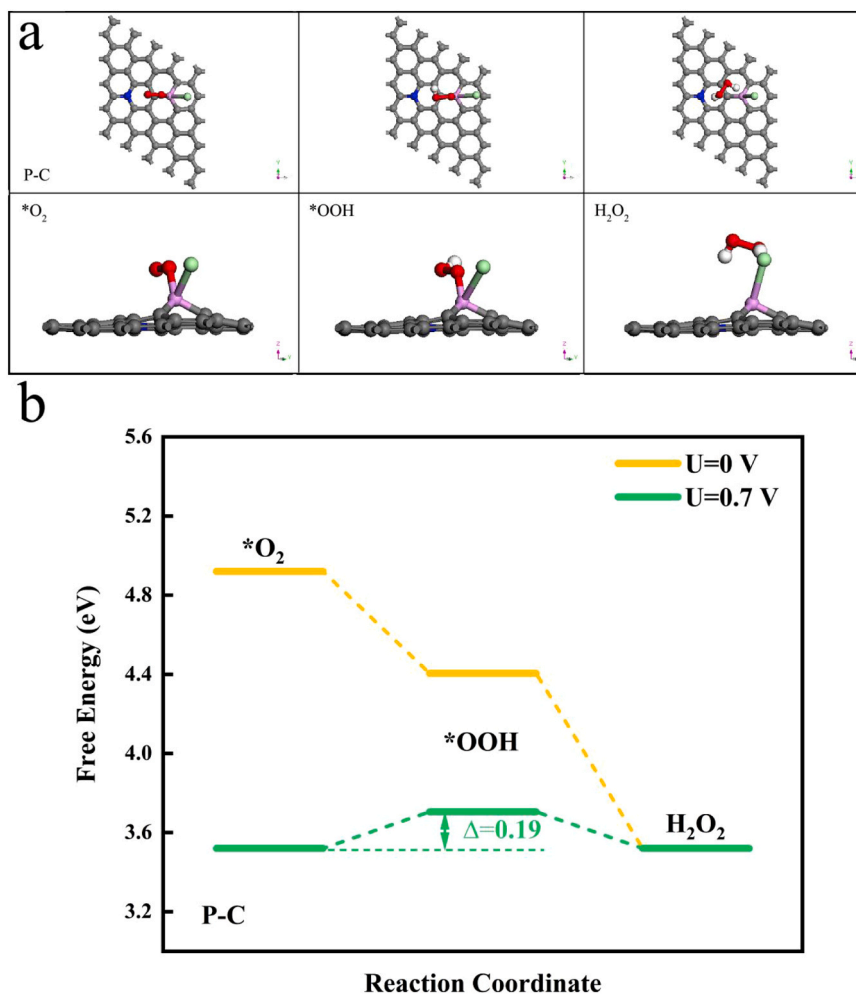

Fig. 7. (a) The most stable configurations of $*O_2$, *OOH, and H_2O_2 on P-C model corresponding to free energy diagram (Atom color notation: gray-C, blue-N, red-O, green-Cl, white-H, pink-P); (b) Free energy diagram for 2e⁻ ORR on P-C after chloride ion adsorption: U= 0 V (yellow line), U= 0.7 V (green line).
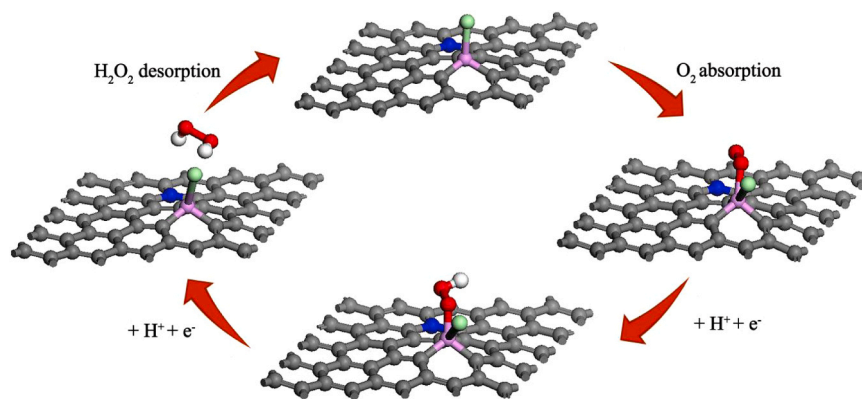
Fig. 8. 2e⁻ ORR process over P-C bond structured catalyst in Cl⁻ containing environment.

4. Conclusion

In summary, a carbon-based catalyst with P-C bond structure was produced by carbonation of EDTMPA, which exhibited enhanced 2e⁻ ORR performance in Cl⁻-containing electrolytes with a synthetic H_2O_2 yield of up to 3.33 mol g^{-1} h^{-1} and a Faraday efficiency of 90.84% at a current density of 100 mA cm^{-2} in a flow-cell electrolytic cell. Based on the structural characterization and DFT calculations, the structure was preferentially occupied by Cl⁻ at the P site in the Cl⁻-containing electrolyte; this process greatly affected the adsorption of O_2 and *OOH on the P-C bond structure, which not only reduced the thermodynamic potential barrier of *O_2 activation but also stabilized the presence of *OOH on the P-C bond structure. In addition, this structure catalyst also had good 2e⁻ ORR performance in real seawater, and the H_2O_2 produced by it in seawater could effectively inactivate marine microorganisms. Our strategy solves the problem of the Fenton reaction to treat the source of H_2O_2 from marine pollution and provides a new direction for the progress of marine environmental protection technology. Moreover, the design of our catalyst fully considers the special usage environment of seawater and transforms Cl⁻, which is harmful to the catalytic reaction, into favorable components to promote the 2e⁻ ORR; therefore, our strategy is also important for the development of catalyst design for use in marine environments.

CRediT authorship contribution statement

Qiuchen He: Conceptualization, Methodology, Experimantal tests, Visualization, Writing – original draft, Writing – review & editing. **Jiangpeng Li:** Experimantal tests. **Yuchen Qiao:** Experimantal tests. **Su Zhan* :** Conceptualization, Methodology, Supervision, Writing – original draft, Writing – review & editing. **Feng Zhou*:** Conceptualization, Supervision, Writing – review & editing, Funding acquisition.

Declaration of Competing Interest

The authors declare that they have no known competing financial interests or personal relationships that could have appeared to influence the work reported in this paper.

Data Availability

No data was used for the research described in the article.

Acknowledgement

Appendix A. Supporting information

Supplementary data associated with this article can be found in the online version at doi:10.1016/j.apcatb.2023.123087.

References

[1] K. Kim, J. Narayanan, A. Sen, S. Chellam, Virus removal and inactivation mechanisms during iron electrocoagulation: capsid and genome damages and electro-fenton reactions, Environ. Sci. Technol. 55 (2021) 13198–13208, https://doi.org/10.1021/acs.est.0c04438.

[2] Z.Y. Liu, W.Q. Huang, C.Q. Huang, Z.Z. Liu, X.Y. Tang, W.C. Chen, Z.Z. Tang, Y.-X. Huang, S.C. Zheng, L. Lin, C. Li, Y. Ye, The construction of high efficient visible-light-driven 3D porous g-C₃N₄/Fe₃O₄ photocatalyst: A new photo-induced bacterial inactivation material enhanced by cascade photo-Fenton reaction, Chemosphere. 312 (2023), 137253, https://doi.org/10.1016/j.chemosphere.2022.137253.

[3] E.S. Okeke, C.O. Okoye, T.P. Chidike Ezeorba, G. Mao, Y. Chen, H. Xu, C. Song, W. Feng, X. Wu, Emerging bio-dispersant and bioremediation technologies as environmentally friendly management responses toward marine oil spill: A comprehensive review, J. Environ. Manag. 322 (2022), 116123, https://doi.org/10.1016/j.jenvman.2022.116123.

[4] Y. Zhang, N. Zhang, T. Wang, H. Huang, Y. Chen, Z. Li, Z. Zou, Heterogeneous degradation of organic contaminants in the photo-Fenton reaction employing pure cubic β-Fe₂O₃, Appl. Catal., B. 245 (2019) 410–419, https://doi.org/10.1016/j.apcatb.2019.01.003.

[5] S. Yang, A. Verdaguer-Casadevall, L. Arnarson, L. Silvioli, V. Čolić, R. Frydendal, J. Rossmeisl, I. Chorkendorff, I.E.L. Stephens, Toward the Decentralized Electrochemical Production of H_2O_2: A Focus on the Catalysis, ACS Catal. 8 (2018) 4064–4081, https://doi.org/10.1021/acscatal.8b00217.

[6] W. Zhou, X. Meng, J. Gao, A.N. Alshawabkeh, Hydrogen peroxide generation from O_2 electroreduction for environmental remediation: A state of the art review, Chemosphere. 225 (2019) 588–607, https://doi.org/10.1016/j.chemosphere.2019.03.042.

[7] J. Gao, H.B. Yang, X. Huang, S.F. Hung, W. Cai, C. Jia, S. Miao, H.M. Chen, X. Yang, Y. Huang, T. Zhang, B. Liu, Enabling Direct H_2O_2 Production in acidic media through rational design of transition metal single atom catalyst, Chem. 6 (2020) 658–674, https://doi.org/10.1016/j.chempr.2019.12.008.

[8] E. Jung, H. Shin, B.H. Lee, V. Efremov, S. Lee, H.S. Lee, J. Kim, W. Hooch Antink, S. Park, K.S. Lee, S.P. Cho, J.S. Yoo, Y.E. Sung, T. Hyeon, Atomic-level tuning of Co–N–C catalyst for high-performance electrochemical H_2O_2 production, Nat. Mater. 19 (2020) 436–442, https://doi.org/10.1038/s41563-019-0571-5.

[9] Y. Sun, L. Silvioli, N.R. Sahraie, W. Ju, J. Li, A. Zitolo, S. Li, A. Bagger, L. Arnarson, X. Wang, T. Moeller, D. Bernsmeier, J. Rossmeisl, F. Jaouen, P. Strasser, Activity–selectivity trends in the electrochemical production of hydrogen peroxide over single-site metal–nitrogen–carbon catalysts, J. Am. Chem. Soc. 141 (2019) 12372–12381, https://doi.org/10.1021/jacs.9b05576.

[10] Q. Zhao, Y. Wang, W.H. Lai, F. Xiao, Y. Lyu, C. Liao, M. Shao, Approaching a high-rate and sustainable production of hydrogen peroxide: oxygen reduction on Co–N–C single-atom electrocatalysts in simulated seawater, Energy Environ. Sci. 14 (2021) 5444–5456, https://doi.org/10.1039/D1EE00878A.

[11] K. Mamtani, D. Jain, A.C. Co, U.S. Ozkan, Investigation of chloride poisoning resistance for nitrogen-doped carbon nanostructures as oxygen depolarized cathode catalysts in acidic media, Catal. Lett. 147 (2017) 2903–2909, https://doi.org/10.1007/s10562-017-2205-3.

[12] J. Yu, B.Q. Li, C.X. Zhao, Q. Zhang, Seawater electrolyte-based metal–air batteries: from strategies to applications, Energy Environ. Sci. 13 (2020) 3253–3268, https://doi.org/10.1039/D0EE01617A.

[13] J. Zhang, H. Zhang, M. Cheng, Q. Lu, Tailoring the electrochemical production of H_2O_2: strategies for the rational design of high-performance electrocatalysts, Small. 16 (2020) 1902845, https://doi.org/10.1002/smll.201902845.

[14] Y. Yang, F. He, Y. Shen, X. Chen, H. Mei, S. Liu, Y. Zhang, A biomass derived N/C-catalyst for the electrochemical production of hydrogen peroxide, Chem. Commun. 53 (2017) 9994–9997, https://doi.org/10.1039/C7CC04819J.

[15] J. Cheng, C. Lyu, H. Li, J. Wu, Y. Hu, B. Han, K. Wu, M. Hojamberdiev, D. Geng, Steering the oxygen reduction reaction pathways of N-carbon hollow spheres by heteroatom doping, Appl. Catal., B. 327 (2023), 122470, https://doi.org/10.1016/j.apcatb.2023.122470.

[16] J. Zhang, G. Zhang, S. Jin, Y. Zhou, Q. Ji, H. Lan, H. Liu, J. Qu, Graphitic N in nitrogen-Doped carbon promotes hydrogen peroxide synthesis from electrocatalytic oxygen reduction, Carbon 163 (2020) 154–161, https://doi.org/10.1016/j.carbon.2020.02.084.

[17] D. Wang, J. Hu, J. Wei, X. Liu, H. Hou, Insights into nitrogen-doped carbon for oxygen reduction: the role of graphitic and pyridinic nitrogen species, ChemPhysChem 24 (2023), 202200734, https://doi.org/10.1002/cphc.202200734.

[18] S. Xin, Y. Li, J. Guan, B. Ma, C. Zhang, X. Ma, W. Liu, Y. Xin, M. Gao, Electrocatalytic oxygen reduction to hydrogen peroxide through a biomass-derived nitrogen and oxygen self-doped porous carbon metal-free catalyst, J. Mater. Chem. A. 9 (2021) 25136–25149, https://doi.org/10.1039/D1TA06955A.

[19] Y. Peng, Z. Bian, Z. Wang, H. Wang, Identifying the key N species for electrocatalytic oxygen reduction reaction on N-doped graphene, Nano Res. 16 (2023) 6642–6651, https://doi.org/10.1007/s12274-023-5421-0.

[20] K.H. Koh, Y.J. Kim, A.H.B. Mostaghim, S. Siahrostami, T.H. Han, Z. Chen, Elaborating nitrogen and oxygen dopants configurations within graphene electrocatalysts for two-electron oxygen reduction, ACS Mater. Lett. 4 (2022) 320–328, https://doi.org/10.1021/acsmaterialslett.1c00660.

[21] T. Sharifi, G. Hu, X. Jia, T. Wågberg, Formation of active sites for oxygen reduction reactions by transformation of nitrogen functionalities in nitrogen-doped carbon nanotubes, ACS Nano. 6 (2012) 8904–8912, https://doi.org/10.1021/nn302906r.

[22] D. Guo, R. Shibuya, C. Akiba, S. Saji, T. Kondo, J. Nakamura, Active sites of nitrogen-doped carbon materials for oxygen reduction reaction clarified using model catalysts, Science. 351 (2016) 361–365, https://doi.org/10.1126/science.aad0832.

[23] H.N. Fernandez-Escamilla, J. Guerrero-Sanchez, E. Contreras, J.M. Ruiz-Marizcal, G. Alonso-Nunez, O.E. Contreras, R.M. Felix-Navarro, J.M. Romo-Herrera, N. Takeuchi, Understanding the selectivity of the oxygen reduction reaction at the atomistic level on nitrogen-doped graphitic carbon materials, Adv. Energy Mater. 11 (2021) 2002459, https://doi.org/10.1002/aenm.202002459.

[24] J. Wu, Z. Yang, X. Li, Q. Sun, C. Jin, P. Strasser, R. Yang, Phosphorus-doped porous carbons as efficient electrocatalysts for oxygen reduction, J. Mater. Chem. A. 1 (2013) 9889, https://doi.org/10.1039/c3ta11849e.

[25] C. Yao, J. Li, Z. Zhang, C. Gou, Z. Zhang, G. Pan, J. Zhang, Hierarchical core–shell Co₂N/CoP embedded in N, P-doped carbon nanotubes as efficient oxygen reduction reaction catalysts for zn-air batteries, Small. 18 (2022) 2108094, https://doi.org/10.1002/smll.202108094.

[26] J. Liu, C. Zhang, S. Yuan, W. Yang, Y. Cao, J. Deng, B. Xu, H. Lu, CoP-decorated N, P-doped necklace-like carbon for highly efficient oxygen reduction and Al-air batteries, Chem. Eng. J. 428 (2022), 131326, https://doi.org/10.1016/j.cej.2021.131326.

[27] Y. Ding, L. Xie, W. Zhou, F. Sun, J. Gao, C. Yang, G. Zhao, Y. Qin, J. Ma, Pulsed electrocatalysis enables the stabilization and activation of carbon-based catalysts towards H₂O₂ production, Appl. Catal., B. 316 (2022), 121688, https://doi.org/10.1016/j.apcatb.2022.121688.

[28] H. Zhang, Y. Li, Y. Zhao, G. Li, F. Zhang, Carbon black oxidized by air calcination for enhanced H₂O₂ generation and effective organics degradation, ACS Appl. Mater. Interfaces. 11 (2019) 27846–27853, https://doi.org/10.1021/acsami.9b07765.

[29] L. Chu, Z. Sun, L. Cang, X. Wang, G. Fang, J. Gao, Identifying the roles of oxygen-containing functional groups in carbon materials for electrochemical synthesis of H₂O₂, J. Environ. Chem. Eng. (2023), 109826, https://doi.org/10.1016/j.jece.2023.109826.

[30] Z. Deng, L. Li, Y. Ren, C. Ma, J. Liang, K. Dong, Q. Liu, Y. Luo, T. Li, B. Tang, Y. Liu, S. Gao, A.M. Asiri, S. Yan, X. Sun, Highly efficient two-electron electroreduction of oxygen into hydrogen peroxide over Cu-doped TiO₂, Nano Res. 15 (2022) 3880–3885, https://doi.org/10.1007/s12274-021-3995-6.

[31] M. Xu, J. Wei, X. Cui, J. Li, G. Pan, Y. Li, Z. Jiang, X. Niu, N. Cui, J. Li, High-efficiency electro-Fenton process based on in-situ grown CoFeCe-LDH@CFs free-standing cathodes: Correlation of cerium and oxygen vacancies on H₂O₂, Chem. Eng. J. 455 (2023), 140922, https://doi.org/10.1016/j.cej.2022.140922.

[32] Z. Wang, Q.K. Li, C. Zhang, Z. Cheng, W. Chen, E.A. McHugh, R.A. Carter, B. I. Yakobson, J.M. Tour, Hydrogen peroxide generation with 100% faradaic efficiency on metal-free carbon black, ACS Catal. 11 (2021) 2454–2459, https://doi.org/10.1021/acscatal.0c04735.

[33] V. Pozzobon, W. Levasseur, E. Viau, E. Michiels, T. Clément, P. Perré, Machine learning processing of microalgae flow cytometry readings: illustrated with Chlorella vulgaris viability assays, J. Appl. Phycol. 32 (2020) 2967–2976, https://doi.org/10.1007/s10811-020-02180-7.

[34] R. Serra-Maia, O. Bernard, A. Gonçalves, S. Bensalem, F. Lopes, Influence of temperature on Chlorella vulgaris growth and mortality rates in a photobioreactor, Algal Res. 18 (2016) 352–359, https://doi.org/10.1016/j.algal.2016.06.016.

[35] W. Mao, M. Li, X. Xue, W. Cao, X. Wang, F. Xu, W. Jiang, Bioaccumulation and toxicity of perfluorooctanoic acid and perfluorooctane sulfonate in marine algae Chlorella sp, Sci. Total Environ. 870 (2023), 161882, https://doi.org/10.1016/j.scitotenv.2023.161882.

[36] M. Jin, S. Liu, G. Meng, S. Zhang, Q. Liu, J. Luo, X. Liu, Low-coordinated Mo clusters for high-efficiency electrocatalytic hydrogen peroxide production, Adv. Mater. Inter. 10 (2023) 2201144, https://doi.org/10.1002/admi.202201144.

[37] N. Jia, T. Yang, S. Shi, X. Chen, Z. An, Y. Chen, S. Yin, P. Chen, N, F-codoped carbon nanocages: an efficient electrocatalyst for hydrogen peroxide electroproduction in alkaline and acidic solutions, ACS Sustain. Chem. Eng. 8 (2020) 2883–2891, https://doi.org/10.1021/acssuschemeng.9b07047.

[38] L. Li, R. Qin, H. Li, L. Yu, Q. Liu, G. Luo, Z. Gao, J. Lu, Functionalized graphene for high-performance two-dimensional spintronics devices, ACS Nano. 5 (2011) 2601–2610, https://doi.org/10.1021/nn102492g.

[39] L.L. Liu, F. Chen, J.H. Wu, M.K. Ke, C. Cui, J.J. Chen, H.Q. Yu, Edge electronic vacancy on ultrathin carbon nitride nanosheets anchoring O₂ to boost H₂O₂ photoproduction, Appl. Catal., B. 302 (2022) 120845, https://doi.org/10.1016/j.apcatb.2021.120845.

[40] J. Hu, C. Chen, H. Yang, F. Yang, J. Qu, X. Yang, W. Sun, L. Dai, C.M. Li, Tailoring well-ordered, highly crystalline carbon nitride nanoarrays via molecular engineering for efficient photosynthesis of H₂O₂, Appl. Catal., B. 317 (2022), 121723, https://doi.org/10.1016/j.apcatb.2022.121723.

[41] T. Li, G. Luo, Q. Liu, S. Li, Y. Zhang, L. Xu, Y. Tang, J. Yang, H. Pang, Encapsulation of NiCo nanoparticles into foam-like porous N, P-codoped carbon nanosheets: Electronic and architectural dual regulations toward high-efficiency water electrolysis, Chem. Eng. J. 410 (2021), 128325, https://doi.org/10.1016/j.cej.2020.128325.

[42] Y. Wang, N. Wei, J. Zeng, Y. Wu, T. Zhou, G. Liu, Q. Liu, J. Guo, Nitrogen-doped carbon nanotube modified ultrafiltration membrane activating peroxymonosulfate for catalytic transformation of phosphonate and mitigation of membrane fouling, Sep. Purif. Technol. 314 (2023), 123522, https://doi.org/10.1016/j.seppur.2023.123522.

[43] R. Javed, H. Zhao, D. Ye, M. Javed, J. Chen, C. Sun, M.A. Khan, L. Chen, L.A. Shah, J. Zhang, Enhancement mechanism of P dopant on atomically distributed FeN₄P-C electrocatalyst over a wide pH range, Electrochim. Acta. 436 (2022), 141452, https://doi.org/10.1016/j.electacta.2022.141452.

[44] Z. Li, A. Kumar, N. Liu, M. Cheng, C. Zhao, X. Meng, H. Li, Y. Zhang, Z. Liu, G. Zhang, X. Sun, Oxygenated P/N co-doped carbon for efficient 2e⁻ oxygen reduction to H₂O₂, J. Mater. Chem. A. 10 (2022) 14355–14363, https://doi.org/10.1039/D2TA02590F.

[45] G. Yu, K. Gong, C. Xing, L. Hu, H. Huang, L. Gao, D. Wang, X. Li, Dual P-doped-site modified porous g-C₃N₄ achieves high dissociation and mobility efficiency for photocatalytic H₂O₂ production, Chem. Eng. J. 461 (2023), 142140, https://doi.org/10.1016/j.cej.2023.142140.

[46] Y. Hu, J. Zhang, T. Shen, Z. Li, K. Chen, Y. Lu, J. Zhang, D. Wang, Efficient electrochemical production of H₂O₂ on hollow N-doped carbon nanospheres with abundant micropores, ACS Appl. Mater. Interfaces. 13 (2021) 29551–29557, https://doi.org/10.1021/acsami.1c05353.

[47] Y. Sun, S. Li, B. Paul, L. Han, P. Strasser, Highly efficient electrochemical production of hydrogen peroxide over nitrogen and phosphorus dual-doped carbon nanosheet in alkaline medium, J. Electroanal. Chem. 896 (2021) 115197, https://doi.org/10.1016/j.jelechem.2021.115197.

[48] J.S. Lim, J.H. Kim, J. Woo, D.S. Baek, K. Ihm, T.J. Shin, Y.J. Sa, S.H. Joo, Designing highly active nanoporous carbon H₂O₂ production electrocatalysts through active site identification, Chem. 7 (2021) 3114–3130, https://doi.org/10.1016/j.chempr.2021.08.007.

[49] S. Kar, K. Bramhaiah, N.S. John, S. Bhattacharyya, Insight into the multistate emissive N, P-doped carbon nano-onions: emerging visible-light absorption for photocatalysis, Chem. Asian J. 16 (2021) 1138–1149, https://doi.org/10.1002/asia.202100137.

[50] G. Li, S. Zheng, L. Wang, X. Zhang, Metal-free chemoselective hydrogenation of nitroarenes by N-doped carbon nanotubes via in situ polymerization of pyrrole, ACS Omega. 5 (2020) 7519–7528, https://doi.org/10.1021/acsomega.0c00328.

[51] J. Yan, H. Li, K. Wang, Q. Jin, C. Lai, R. Wang, S. Cao, J. Han, Z. Zhang, J. Su, K. Jiang, Ultrahigh phosphorus doping of carbon for high-rate sodium ion batteries anode, Adv. Energy Mater. 11 (2021) 2003911, https://doi.org/10.1002/aenm.202003911.

[52] X. Jiao, Y. Liu, B. Li, W. Zhang, C. He, C. Zhang, Z. Yu, T. Gao, J. Song, Amorphous phosphorus-carbon nanotube hybrid anode with ultralong cycle life and high-rate capability for lithium-ion batteries, Carbon. 148 (2019) 518–524, https://doi.org/10.1016/j.carbon.2019.03.053.

[53] X. Yan, S. Huang, F. Wang, S. Sun, G. Zhang, B. Jiang, B. Zhang, S. Che, W. Yang, Y. Li, Enhanced catalytic hydrogen evolution reaction performance of highly dispersed Ni₂P nanoparticles supported by P-doped porous carbon, Colloids Surf., A. 616 (2021) 126308, https://doi.org/10.1016/j.colsurfa.2021.126308.

[54] D. Radziuk, H. Möhwald, Ultrasonically treated liquid interfaces for progress in cleaning and separation processes, Phys. Chem. Chem. Phys. 18 (2016) 21–46, https://doi.org/10.1039/C5CP05142H.

[55] J. Wu, X. Zheng, C. Jin, J. Tian, R. Yang, Ternary doping of phosphorus, nitrogen, and sulfur into porous carbon for enhancing electrocatalytic oxygen reduction, Carbon. 92 (2015) 327–338, https://doi.org/10.1016/j.carbon.2015.05.013.

[56] S.H. Daryan, J. Javadpour, A. Khavandi, M. Erfan, Morphological evolution on the surface of hydrothermally synthesized hydroxyapatite microspheres in the presence of EDTMP, Ceram. Int. 44 (2018) 19743–19750, https://doi.org/10.1016/j.ceramint.2018.07.229.

[57] J. Peng, Y. Sun, L. Zhao, Y. Wu, W. Feng, Y. Gao, F. Li, Polyphosphoric acid capping radioactive/upconverting NaLuF4:Yb,Tm,153Sm nanoparticles for blood pool imaging in vivo, Biomaterials. 34 (2013) 9535–9544, https://doi.org/10.1016/j.biomaterials.2013.07.098.

[58] M.A. Patel, F. Luo, M.R. Khoshi, E. Rabie, Q. Zhang, C.R. Flach, R. Mendelsohn, E. Garfunkel, M. Szostak, H. He, P-doped porous carbon as metal free catalysts for selective aerobic oxidation with an unexpected mechanism, ACS Nano. 10 (2016) 2305–2315, https://doi.org/10.1021/acsnano.5b07054.

[59] B. Ochiai, Y. Sano, T. Endo, Synthesis and Crosslinking of Oligo (carbonate-ketone) Obtained by Radical Polymerization of 4-methylene-5,5-dimethyl-1,3-dioxolan-2-one, Networkpolymer. 26 (2005) 132–137, https://doi.org/10.11364/networkpolymer1996.26.132.

[60] A.H. Sulaymon, Column biosorption of lead, cadmium, copper, and arsenic ions onto algae, Environ. Sci. Pollut. Res. 20 (2013) 3011–3023, https://doi.org/10.1007/s11356-012-1208-2.

[61] J. Lei, Y. Yao, Y. Huang, Y.C. Lu, A highly reversible low-cost aqueous sulfur–manganese redox flow battery, ACS Energy Lett. 8 (2023) 429–435, https://doi.org/10.1021/acsenergylett.2c02524.

[62] H. Yang, S. Gao, D. Rao, X. Yan, Designing superior bifunctional electrocatalyst with high-purity pyrrole-type CoN_4 and adjacent metallic cobalt sites for rechargeable Zn-air batteries, Energy Storage Mater. 46 (2022) 553–562, https://doi.org/10.1016/j.ensm.2022.01.040.

[63] J. Zhang, T. Zhang, J. Ma, Z. Wang, J. Liu, X. Gong, ORR and OER of Co-N codoped carbon-based electrocatalysts enhanced by boundary layer oxygen molecules transfer, Carbon. 172 (2021) 556–568, https://doi.org/10.1016/j.carbon.2020.10.075.

[64] X. Yu, S. Lai, S. Xin, S. Chen, X. Zhang, X. She, T. Zhan, X. Zhao, D. Yang, Coupling of iron phthalocyanine at carbon defect site via π-π stacking for enhanced oxygen reduction reaction, Appl. Catal. B. 280 (2021), 119437, https://doi.org/10.1016/j.apcatb.2020.119437.

[65] L. Li, P. Dai, X. Gu, Y. Wang, L. Yan, X. Zhao, High oxygen reduction activity on a metal–organic framework derived carbon combined with high degree of graphitization and pyridinic-N dopants, J. Mater. Chem. A. 5 (2017) 789–795, https://doi.org/10.1039/C6TA08016B.

[66] Z. Li, J. Zou, X. Xi, P. Fan, Y. Zhang, Y. Peng, D. Banham, D. Yang, A. Dong, Native ligand carbonization renders common platinum nanoparticles highly durable for electrocatalytic oxygen reduction: annealing temperature matters, Adv. Mater. 34 (2022) 2202743, https://doi.org/10.1002/adma.202202743.

[67] K. Ono, Y. Yasuda, K. Sekizawa, N. Takeuchi, T. Yoshida, M. Sudoh, Evaluation of Pt/C catalyst degradation and H_2O_2 formation changes under simulated PEM fuel cell condition by a rotating ring-disk electrode, Electrochim. Acta. 97 (2013) 58–65, https://doi.org/10.1016/j.electacta.2013.02.070.

[68] K. Ke, T. Hatanaka, Y. Morimoto, Reconsideration of the quantitative characterization of the reaction intermediate on electrocatalysts by a rotating ring-disk electrode: The intrinsic yield of H_2O_2 on Pt/C, Electrochim. Acta. 56 (2011) 2098–2104, https://doi.org/10.1016/j.electacta.2010.11.086.

[69] S. Chen, T. Luo, K. Chen, Y. Lin, J. Fu, K. Liu, C. Cai, Q. Wang, H. Li, X. Li, J. Hu, H. Li, M. Zhu, M. Liu, Chemical identification of catalytically active sites on oxygen-doped carbon nanosheet to decipher the high activity for electro-synthesis hydrogen peroxide, Angew. Chem. 133 (2021) 16743–16750, https://doi.org/10.1002/ange.202104480.

[70] J. Quílez-Bermejo, A. Ghisolfi, D. Grau-Marín, E. San-Fabián, E. Morallón, D. Cazorla-Amorós, Post-synthetic efficient functionalization of polyaniline with phosphorus-containing groups. Effect of phosphorus on electrochemical properties, Eur. Polym. J. 119 (2019) 272–280, https://doi.org/10.1016/j.eurpolymj.2019.07.048.

[71] S. Hu, Q. Chang, K. Lin, J. Yang, Tailoring surface charge distribution of carbon dots through heteroatoms for enhanced visible-light photocatalytic activity, Carbon. 105 (2016) 484–489, https://doi.org/10.1016/j.carbon.2016.04.078.

[72] X. Wang, J. Wang, P. Wang, L. Li, X. Zhang, D. Sun, Y. Li, Y. Tang, Y. Wang, G. Fu, Engineering 3d-2p-4f Gradient Orbital Coupling to Enhance Electrocatalytic Oxygen Reduction, Adv. Mater. 34 (2022) 2206540, https://doi.org/10.1002/adma.202206540.

[73] C. Wu, M. Yin, R. Zhang, Z. Li, Z. Zou, Z. Li, Further studies of photodegradation and photocatalytic hydrogen production over Nafion-coated Pt/P25 sensitized by rhodamine B, Int. J. Hydrog. Energy. 45 (2020) 22700–22710, https://doi.org/10.1016/j.ijhydene.2020.06.098.

[74] B.C. Kang, B.S. Park, T.J. Ha, Highly sensitive wearable glucose sensor systems based on functionalized single-wall carbon nanotubes with glucose oxidase-nafion composites, Appl. Surf. Sci. 470 (2019) 13–18, https://doi.org/10.1016/j.apsusc.2018.11.101.

[75] A. Thiam, R. Salazar, E. Brillas, I. Sirés, In-situ dosage of Fe^{2+} catalyst using natural pyrite for thiamphenicol mineralization by photoelectro-Fenton process, J. Environ. Manag. 270 (2020), 110835, https://doi.org/10.1016/j.jenvman.2020.110835.

[76] A. Olabi, S. Yildiz, Sludge disintegration using UV assisted Sono-Fenton process, Environ. Sci. Pollut. Res. 28 (2021) 52565–52575, https://doi.org/10.1007/s11356-021-14505-1.